



RESEARCH ARTICLE

10.1002/2017GC007107

Microseismicity Linked to Gas Migration and Leakage on the Western Svalbard Shelf

Peter Franek¹ , Andreia Plaza-Faverola¹ , Jürgen Mienert¹, Stefan Buenz¹, Bénédicte Ferré¹, and Alun Hubbard¹ 

¹Centre for Arctic Gas Hydrate, Environment and Climate, Department of Geosciences, UiT The Arctic University of Norway, Tromsø, Norway

Key Points:

- An ocean bottom seismometer was deployed to record microseismicity in marine sediments
- An automated algorithm is applied to detect 220,000 short duration events (<1 s) which occurrence vary over ~10 day and seasonal time scales
- We infer that two distinct types of events originate from marine macrofauna vocalization and from fluid migration and natural gas seepage

Supporting Information:

- Supporting Information S1
- Table S1

Correspondence to:

P. Franek,
peter.franek@uit.no

Citation:

Franek, P., Plaza-Faverola, A., Mienert, J., Buenz, S., Ferré, B., & Hubbard, A. (2017). Microseismicity linked to gas migration and leakage on the Western Svalbard Shelf. *Geochemistry, Geophysics, Geosystems*, 18, 4623–4645. <https://doi.org/10.1002/2017GC007107>

Received 7 JUL 2017

Accepted 2 DEC 2017

Accepted article online 7 DEC 2017

Published online 26 DEC 2017

© 2017. The Authors.

This is an open access article under the terms of the Creative Commons Attribution-NonCommercial-NoDerivs License, which permits use and distribution in any medium, provided the original work is properly cited, the use is non-commercial and no modifications or adaptations are made.

Abstract The continental margin off Prins Karls Forland, western Svalbard, is characterized by wide-spread natural gas seepage into the water column at and upslope of the gas hydrate stability zone. We deployed an ocean bottom seismometer integrated into the MASOX (Monitoring Arctic Seafloor-Ocean Exchange) automated seabed observatory at the pinch-out of this zone at 389 m water depth to investigate passive seismicity over a continuous 297 day period from 13 October 2010. An automated triggering algorithm was applied to detect over 220,000 short duration events (SDEs) defined as having a duration of less than 1 s. The analysis reveals two different types of SDEs, each with a distinctive characteristic seismic signature. We infer that the first type consists of vocal signals generated by moving mammals, likely finback whales. The second type corresponds to signals with a source within a few hundred meters of the seismometer, either due east or west, that vary on short (~tens of days) and seasonal time scales. Based on evidence of prevalent seafloor seepage and subseafloor gas accumulations, we hypothesize that the second type of SDEs is related to subseafloor fluid migration and gas seepage. Furthermore, we postulate that the observed temporal variations in microseismicity are driven by transient fluid release and due to the dynamics of thermally forced, seasonal gas hydrate decomposition. Our analysis presents a novel technique for monitoring the duration, intensity, and periodicity of fluid migration and seepage at the seabed and can help elucidate the environmental controls on gas hydrate decomposition and release.

1. Introduction

Short impulsive signals (microseismic events) with frequencies >1–2 Hz are regularly recorded by ocean bottom seismometers (OBS). However, such seismic events, which are common in many offshore seismic monitoring records, have an uncertain origin. They are often attributed to biological sources when marine animals interact with the instrument (e.g., Buskirk et al., 1981, who refer to “fish bumps”), and hence, are for the most part disregarded as noise. Several nonbiological signature types have also been proposed though. These include hydraulic fracturing and vibrating fluid generated by pressure pulses within hydrothermal system (e.g., Sohn et al., 1995) or resonance of fluid-filled conduits excited by sudden pressure transients (e.g., Díaz et al., 2007). Seismic events of short duration have also been associated with bubbling when observed at onshore settings, for example, at Dashgil mud volcano in Azerbaijan (Albarelo et al., 2012). Moreover, fluid migration toward the seafloor and subsequent natural gas emissions—gas seepage—has been proposed to explain observations of microseismic events at the Niger Delta (Sultan et al., 2011), the Sea of Marmara (Tary et al., 2012), and the Håkon Mosby mud volcano in the Barents Sea (Franek et al., 2014). In this latter study, the interpretation of gas seepage as a source of microseismicity was inferred from the close correlation of the microseismic events with both acoustic flares (Bayrakci et al., 2014) and abrupt increases in dissolved methane concentration observed in the water column (Embriaco et al., 2014). Both observations imply extensive, localized natural gas seepage from the seafloor which occurred synchronously with episodes of enhanced microseismicity.

Here we present observations of microseismic events recorded at a site on the western margin of Svalbard where natural methane is actively seeping from the seafloor of the upper continental slope between 80 and 400 m depth (e.g., Ferré et al., 2012; Sahling et al., 2014; Westbrook et al., 2009). An OBS was integrated into the MASOX (Monitoring Arctic Seafloor-Ocean Exchange) automated seabed observatory deployed by the University of Tromsø for long-term measurements as part of an Arctic Ocean ESONET (European Seas

Observatory NETWORK) Mission. The main objective of the observatory was to monitor fluid release activity from the seafloor and to determine an effect of warming shallow Arctic waters on the thermodynamic conditions of the gas (methane) hydrate stability zone (Berndt et al., 2014; Person et al., 2015).

The location of MASOX observatory was carefully selected at 389 m depth to fall just inside the upper pinch-out of the gas hydrate stability zone (Westbrook et al., 2009). Berndt et al. (2014) documented seasonal bottom water temperature fluctuations in the area and hypothesized that there is a strong seasonal control on gas hydrate formation and dissociation along with any seepage of methane from the seafloor at this site. Investigating microseismicity potentially associated with gas leakage from the seafloor can advance the understanding of the dynamics of these systems, particularly through assessment of the duration, intensity, and periodicity of seepage into the water column. This can provide constrains on the properties of leakage structures which is particularly important for risk assessment and monitoring strategies of gas injections associated with CO₂ storage (e.g., Stork et al., 2015; Tanase et al., 2013). Moreover, analysis of distinct sub-bottom microseismic signatures can help constraining the rates of methane release into the ocean and its controlling mechanisms. Widespread methane release to the oceans can significantly alter the global carbon cycle, having important implications as, for example, for ocean acidification, climate, and seabed ecology (e.g., Biastoch et al., 2011; Dickens, 2003; Isaksen et al., 2011; Pohlman et al., 2011). Constraining processes involved with seafloor seepage is thus a fundamental requirement to advance the understanding of these complex interactions.

2. Study Area

The study is focused on a 25 by 55 km zone of active seafloor seepage restricted to the shelf edge of the west Svalbard passive margin (Figure 1). The MASOX observatory was deployed on the seafloor ~32 km west of Prins Karls Forland at a depth of 389 m (Figure 1). The west Svalbard continental margin was formed as a result of continental breakup and seafloor spreading between the Greenland and Fennoscandian

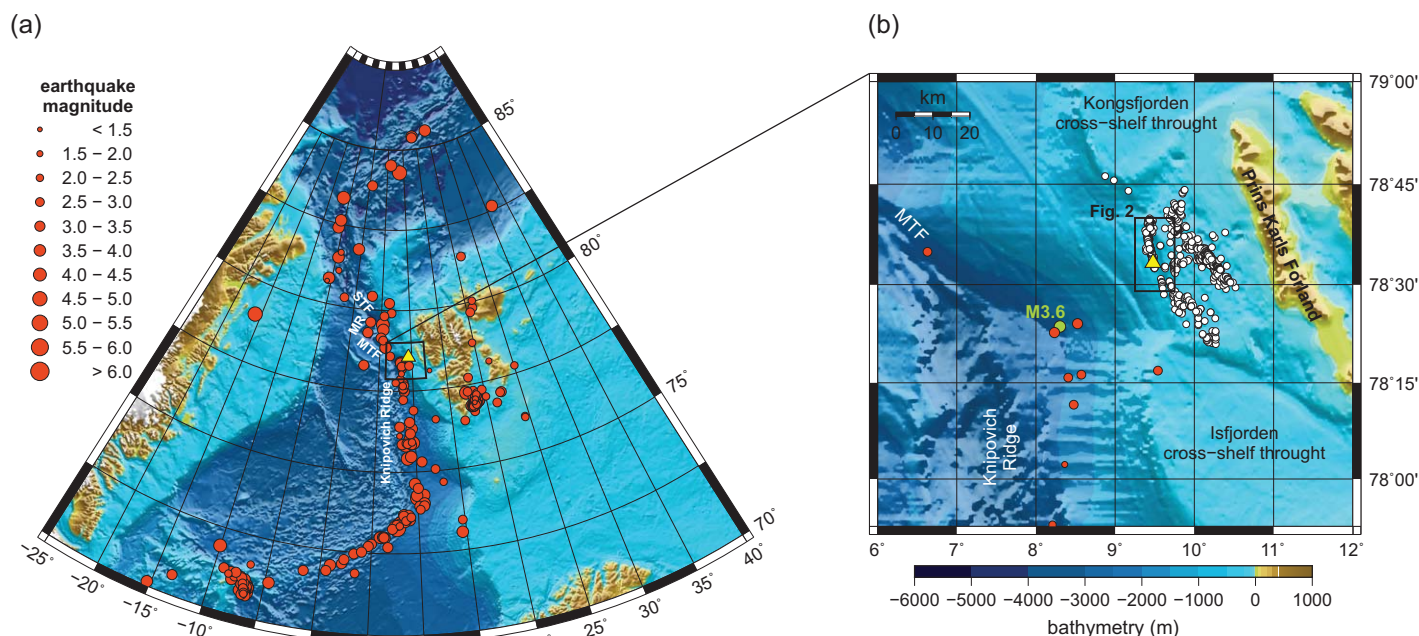


Figure 1. (a) Bathymetry map showing location of the MASOX site (yellow triangle) at position of 78°33'16.936"N, 9°28'38.568"E on the west Svalbard continental margin off Prins Karls Forland. Epicenters of earthquakes that were identified in the seismic record during operational period of the OBS from 13 October 2010 to 31 July 2011 are represented by red circles with size scaled to the magnitude of events. The earthquake locations are extracted from the Reviewed Bulletin of the International Seismic Center (<http://www.isc.ac.uk>) and from the NORSAR regional reviewed bulletin (<http://www.norsar.no/NDC/bulletins/regional>) (supporting information Table S1). (b) Close-up on the study area with the MASOX site. Light-green circle indicates position of an earthquake which seismic record is shown in Figure 3 White circles are mapped seep sites (acoustic flares) (e.g., Graves et al., 2015; Sahling et al., 2014; Veloso et al., 2015). MR = Molloy Ridge, MTF = Molloy Transform Fault, STF = Spitsbergen Transform Fault.

continental blocks during the early Eocene (e.g., Eldholm et al., 1987; Faleide et al., 1993; Mosar et al., 2002). Since the onset of the Pleistocene ~2.7 Ma ago, this continental margin has been dissected and sculpted by numerous glacial episodes in which an extensive marine-based ice sheet advanced over the Svalbard and the Barents Sea (e.g., Ingólfsson & Landvik, 2013; Landvik et al., 2005; Ottesen et al., 2005; Patton et al., 2015; Svendsen et al., 1992). Fast flowing ice streams draining the ice sheet caused major incision and glacial erosion into the shelf creating the Kongsfjorden cross-shelf trough in the north and the Isfjorden cross-shelf trough in the south. Ice streams also transported large volume of sediments which were deposited as prograding glacial debris flow units at the heads of the troughs. Intertrough zones were characterized by slow flowing ice that was frozen to its bed and hence led to the preservation of older sediment formations (Landvik et al., 2005).

Although it is currently a passive continental margin, the shelf-break offshore western Svalbard is located within ~40 km from the active spreading ridges and transform segments of the Fram Strait (Figure 1). Hence, the western Svalbard margin is subject to ongoing tectonic activity from the Spitsbergen Transform Fault, the Molloy Ridge, the Molloy Transform Fault, and the northward propagation of the Knipovich Ridge

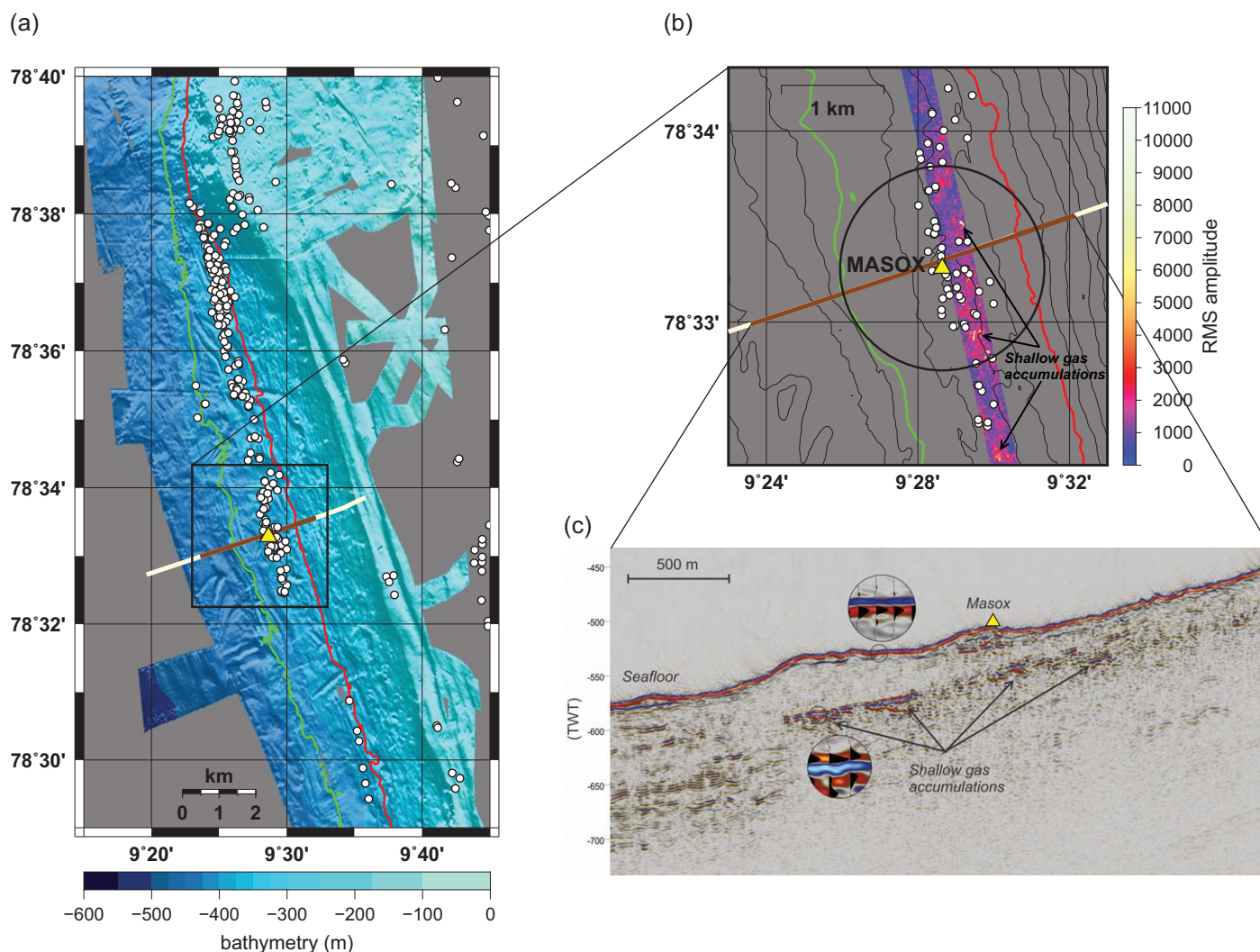


Figure 2. (a) Detailed bathymetry of the study area. Red and green lines are bathymetric contours at 370 and 410 m water depth and represent the upper pinch-out of the gas hydrate stability zone at 2°C and 3°C bottom water temperature, respectively, modeled by Sarkar et al. (2012). White circles are mapped seep sites (acoustic flares) and yellow triangle indicates location of the MASOX site. The white is the outline of a 2-D seismic profile and in brown is the part of the seismic transect shown in Figure 2c. (b) Dip map (10 m spaced bathymetric lines) with projected RMS amplitude map from the P-cable 3-D seismic data enhancing a high amplitude anomaly at ~50 ms beneath the seafloor. Distance (1,000 m) from the MASOX site is indicated by black circle. (c) Seismic profile showing the upslope distribution of the high amplitude anomaly in Figure 2b indicating gas accumulation beneath the MASOX site.

(Crane et al., 2001; Peive & Chamov, 2008). Furthermore, the western Svalbard continental shelf has undergone flexural rebound and glacio-isostatic uplift associated with the ultimate episode of retreat of the Barents Sea and Fennoscandian ice-sheets (e.g., Auriac et al., 2016; Johnston, 1989; Stewart et al., 2000).

Ongoing seismic activity in the area is—for the most part—moderate, with primary earthquake locations predominantly aligned along the active plate boundaries interspersed with the occasional intraplate earthquake (Figure 1) (Dehls et al., 2000; Engen et al., 2003). Known focal mechanism solutions (International Seismic Center, Reference Event Bulletin, <http://www.isc.ac.uk>) confirm ongoing extensional faulting at the Knipovich Ridge and dextral strike-slip faulting at the Molloy Transform Fault (Plaza-Faverola et al., 2015).

Across the continental shelf, fluid migration and natural gas release from the seafloor have been observed at water depths ranging between 80 and 400 m (Gentz et al., 2014; Sahling et al., 2014; Veloso et al., 2015; Westbrook et al., 2009). Seepage occurs at and upslope of the intersection of the present gas hydrate stability zone with the seafloor at around 400 m water depth (Figure 2a) (e.g., Westbrook et al., 2009). Anomalous seismic velocities provide geophysical evidence for the presence of shallow gas accumulations (Figures 2b and 2c) underlying presumed gas hydrate bearing sediments (Chabert et al., 2011; Sarkar et al., 2012). Gas migration from deep thermogenic reservoirs to the seafloor through vertical pathways is speculated to be one of the primary mechanisms sustaining seepage (Rajan et al., 2012; Westbrook et al., 2009). Vertical transport of the gas and fluids can also be diverted laterally by upslope rising sedimentary strata combined with the buildup of blocking gas hydrates (Rajan et al., 2012; Sarkar et al., 2012), which form in the shallow sediments when upward migrating gas-rich fluids attain the stability zone. Since the stability envelope for gas hydrates is dependent on ambient temperature and pressure conditions, any warming of bottom water temperature will result in short-term destabilization of hydrates and subsequent release and seepage of natural gas (Berndt et al., 2014; Ferré et al., 2012; Graves et al., 2015; Thatcher et al., 2013; Westbrook et al., 2009) that may ultimately reach the atmosphere (Shakhova et al., 2010). This effect is enhanced in the Arctic regions (Biaostoch et al., 2011) where temperature fluctuations due to the West Spitsbergen Current that transports warm Atlantic Water northward along the shelf edge are significant—even at shallow water depths—and can drive enhanced gas hydrate dissociation (Ferré et al., 2012; Schauer et al., 2004; Spielhagen et al., 2011; Steinle et al., 2015).

3. Instrumentation and Data

3.1. OBS Records

The MASOX seafloor observatory includes an OBS system which consists of a three-component K/MT seismometer (corner frequency 4.5 Hz) and a hydrophone (corner frequency 0.01 Hz). The entire instrument array was deployed for 297 days from 13 October 2010 to 5 August 2011. The OBS was preset in continuous recording mode with a sample rate of 20 ms (50 Hz) and operated seamlessly throughout the deployment period. It provides a time series of ground acceleration at 16 bit precision in the vertical (component Z) and two orthogonal horizontal directions (components H1 and H2) with an unknown initial orientation since the OBS was not equipped with any directional sensor. Leveling of the OBS was accommodated during the deployment of the MASOX observatory with the assistance of underwater video camera to position the system on a flat part of the seafloor. Seismic records were band-pass filtered using a Butterworth filter in the range of 1.5–24 Hz to eliminate undesirable frequency signals (e.g., ocean microseisms, instrumental noise). The seismograms were not corrected for instrument response because of the unknown transfer function of the seismometer. Review of the hydrophone data revealed systematic high noise level throughout the operational period, even when strong *T* waves due to earthquakes were registered by the seismometer. It is hence presumed that the hydrophone malfunctioned or was not properly set up.

3.2. Earthquakes

Known earthquakes that occurred during the 10 month operational period with epicenters within the domain bounded from 25°W to 40°E and 70°N to 90°N were collated and compiled into a catalog (supporting information Table S1). Parameters of the earthquakes (longitude, latitude, hypocentral depth, origin time, and magnitude) were extracted from the Reviewed Bulletin of the International Seismic Center (<http://www.isc.ac.uk>) and from the NORSAR regional reviewed bulletin (<http://www.norsardata.no/NDC/bulletins/regional>). Compiled data were parsed, quality assessed, and duplicate events were removed. In a set of duplicate events, events from the Reviewed Bulletin of the International Seismic Center were retained in

expected arrival times and 265 distinct earthquake signatures from 286 earthquakes in the catalog were identified in the record (Figure 1a).

All identified earthquake signatures in the seismic record included *P* waves, but *S* waves (Figure 3) were not consistently present and only apparent for events with an epicenter distance of less than ~ 250 km. This is to be expected given that *S* waves usually undergo greater attenuation than *P* waves over long distances. Moreover, the seismic record, particularly in the horizontal components, may also be affected by weak coupling of the seismometer to the seafloor (e.g., Osler & Chapman, 1998, and references therein). Despite this, unambiguous *S* waves originating from local earthquakes verify that the OBS was well coupled to the seafloor and fully capable of registering both *S* and *P* waves. For example, a clear *S* wave arrival can be identified in the seismic record of a local earthquake, magnitude $M = 3.6$, located with an epicenter ~ 32 km from the MASOX site (Figure 3; earthquake No. 183 in supporting information Table S1). For this earthquake, *P* and *S* wave have maximum energy in the frequency range ~ 2 –5 Hz and ~ 2 –10 Hz, respectively, but also contain higher-frequencies presumably due to the proximity to the source. The *P* and *S* wave arrivals are followed by converted and scattered waves likely originating from heterogeneities in the rock and sedimentary stratigraphy through which waves propagated. Surface waves supposedly follow the *S* wave, however, their frequencies might be out the frequency range of seismometer and therefore are difficult to identify.

4. Analysis and Results

4.1. Orientation of Horizontal Components of the OBS

The orientation of components H1 and H2 relative to the geographic north (Figure 4a) was determined through a polarization analysis of earthquake generated *P* waves (e.g., Montalbetti & Kanasevich, 1970). Both mean value and linear trend were removed from seismic records of the earthquakes, and a 2–6 Hz Butterworth filter was applied to isolate earthquake generated *P* waves from all other signals (cf. Figure 3). The horizontal motion of *P* waves was then manually picked to determine the apparent back azimuth (i.e., an angle of impinging seismic wave measured clockwise from an arbitrarily chosen horizontal component, we opt the component H2). As the direction of the horizontal particle motion of *P* waves corresponds to the propagation direction of the seismic waves, the apparent back azimuths were combined with station-to-earthquake azimuths to calculate the angle of rotation on the horizontal axes (Figure 4a). Implicit to this procedure is an orientation ambiguity of $\pm 180^\circ$ that was resolved by accounting for the polarity of the *P* wave's first motion in the vertical component *Z*. A supplementing description of the procedure is given in supporting information Text S1 and Figure S1.

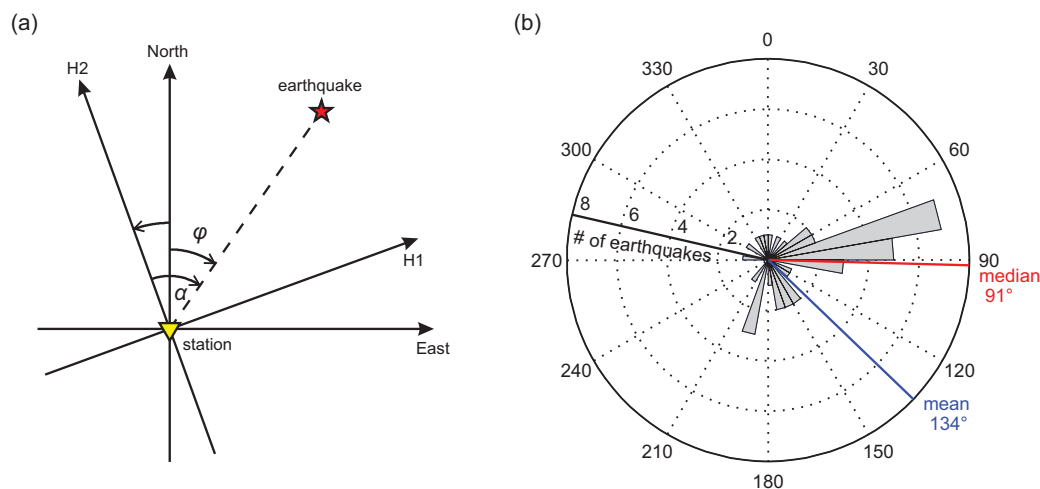


Figure 4. (a) EW–NS coordinate system and H1–H2 coordinate system defined by horizontal components of the seismometer. Apparent back azimuth α , which was determined by polarization analysis of *P* wave, and station-to-earthquake azimuth φ define seismometer orientation $\vartheta = \alpha - \varphi$. Arrows indicate orientation of angles, clockwise orientation means positive angles. (b) Distribution of the seismometer orientations ϑ determined by using 40 earthquake records. Mean and median values of the distribution are indicated by blue and red color, respectively.

The onset of *P* waves for a large majority of identified earthquakes was emergent, which in these cases precludes any determination of the first motion polarity (upward or downward). However, after careful screening of all recognized events, 40 earthquakes out of 265 (supporting information Table S1) provided sufficiently strong *P* waves with reliable first motion onset to adequately constrain polarization analysis. The resulting distribution of angles of rotation has several maxima, with the largest between 70° and 100° (Figure 4b). The fragmented distribution is possibly due to the presence of noise signals overlapping the frequency range of filtered seismic *P* wave records, resulting in weaker or distorted polarization of *P* waves (cf. supporting information Figure S2). A median value of 91° corresponds with the largest maximum of distribution and this rotation is applied to the horizontal components to obtain N (north-south) and E (east-west) components of the OBS (Figure 4b).

4.2. Short Duration Events

Visual inspection of the OBS records reveals the presence of many seismic events of duration <1 s (Figure 5) that we refer to as short duration events (SDEs) following Díaz et al. (2007). An automated approach to identifying SDEs is used by applying a short-time average/long-time average (STA/LTA) algorithm to the seismic record. The STA/LTA algorithm is computationally efficient and widely used for automated earthquake identification but requires judicious parameter selection. There are several modifications of the algorithm (e.g., Allen, 1978; Baer & Kradolfer, 1987; Earle & Shearer, 1994; Trnkoczy, 2012), each suited to particular applications, but all can be prone to missing some events and the artificial generation of false triggers. The STA/LTA approach adopted here continuously evaluates the ratio between short-term and long-term averages of amplitudes determined from all three components. If the ratio exceeds a predefined threshold value and its duration is shorter than 1 s, then a SDE is identified and logged. A suite of parameter sets for the STA and LTA window duration and the trigger threshold level were tested on a randomly selected 1 h window. Parameters of 0.2 s for the STA, 4.0 s for the LTA, and 6 for the threshold level yield optimal results. For these values, the greatest number of SDEs (20) within the 1 h window was correctly identified consistent with those from visual inspection without any false triggers (Figure 5).

When applied to the entire 297 day OBS seismic record, over 220,000 SDEs were detected by the STA/LTA algorithm yielding a mean rate of 32 events per hour. The strongest SDEs (several hundreds) were visually inspected and six distinct yet typical examples of the vertical component of these SDEs together with their spectrograms are presented (Figure 6). The SDEs presented in Figure 6 have durations of 0.2–1.0 s with variable amplitudes and frequencies higher than ~3 Hz with one or several distinctive peaks. The first SDE presented appears to be composed of a single wavelet (Figure 6a) which has a broad frequency content from ~3 to ~20 Hz. Other SDEs (Figures 6b and 6e) show more complex waveforms likely resulting from the combined effect of wave reflections, conversions, and complexity of source mechanism. Some of the SDEs (Figures 6c and 6e) have well-separated frequency peaks at ~3–5 and ~10–17 Hz, possibly due to a resonance in the upper seafloor sediments caused by incoming seismic waves. However, since such separated frequency peaks are not present in all SDEs, a specific source dependent mechanism cannot be discounted. In several cases, small amplitude wave follows the SDE (indicated in Figures 6a and 6c as reflected wave). Differences in arrival times between larger and smaller waves (the cases shown in Figures 6a and 6c and others not shown here) were systematically from ~0.5 up to ~2 s. For a seismic source located at the OBS at 389 m water depth, the shortest difference of direct and reflected wave arrivals is ~0.5 s assuming a sound speed in water of 1500 m/s. Therefore, we interpret these small amplitude waves as reflections from the sea surface. The SDE presented in Figure 6f is characterized by a strong and relatively narrow frequency peak between 17 and 23 Hz, and is separately analyzed in the following section 4.3.

In all cases of SDEs, separate arrivals of *P* and *S* waves are not recognized. This is either due to both of them overlapping, amplitudes of *P* waves being at the level of noise and thus SDEs are *S* waves, or *S* waves being entirely absent. In detail, irregular particle motion (supporting information Figure S3) of the representative examples of SDEs from Figure 6 confirms complexity of the SDEs waveforms, though, in most cases it is highly rectilinear (rectilinearity as defined by Jurkevics, 1988 is for shown examples >0.85 except in one case when ~0.73) meaning that either *P* or *S* waves are present. Comparing *S* wave of the presented earthquake with some of the strongest SDEs (Figure 3 versus Figures 6a–6d) demonstrates that magnitudes of their amplitudes are similar. Then *P* waves are likely to be recognized in several cases at the assumption—given the large number of SDEs—that the ratio between radiated energy in *P* and *S* waves is comparable between the known earthquake and some of the visually inspected SDEs. However, this is not the case and

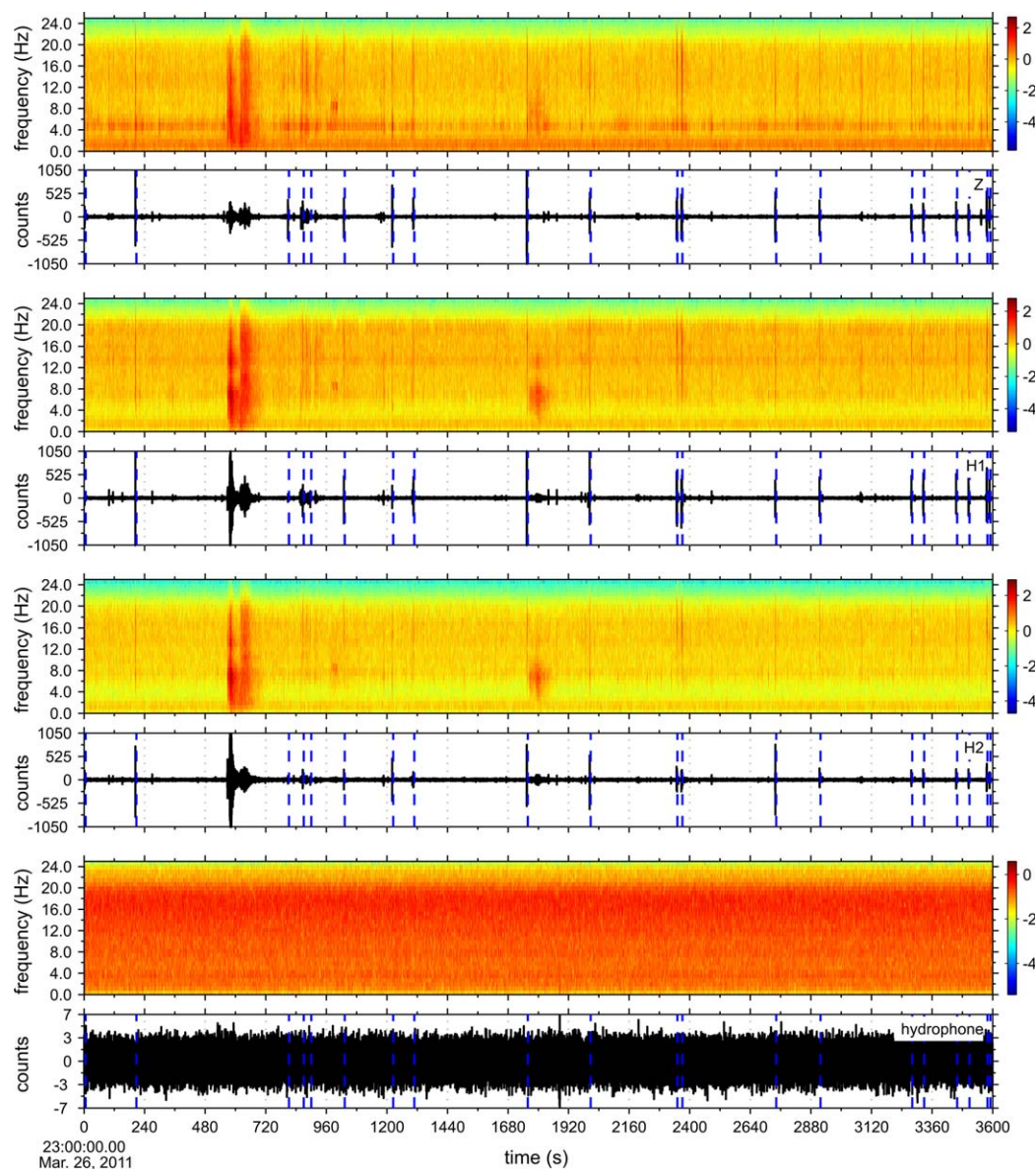


Figure 5. One hour record of the vertical component Z, two horizontal components H1 and H2 and the hydrophone showing an earthquake at ~600 s and numerous short duration events (SDEs). The starting time of the records corresponds to 26 March 2011, 23:00:00. Above every record is shown its spectrogram in $\log(\text{counts}^2/\text{Hz})$ units calculated by short-time Fourier transform (frame length 1.0 s, 50% overlap, Tukey window with 0.5 s total length of tapered section). Blue dashed lines indicate the SDEs recognized by the STA/LTA algorithm that was adapted for identifying events with duration less than 1 s. Most of the SDEs were identified by the STA/LTA algorithm (20 events), but the earthquake was not recognized as an event. The hydrophone record shows only noise signal. All records were filtered with band-pass Butterworth filter in the frequency range 1.5–24 Hz.

thus we infer for the SDEs being mostly *P* waves. Rather large incident angles that may be deduced from the particle motion of presented SDEs in vertical planes (supporting information Figure S3), can be interpreted as due to very shallow depth of their sources in the case of only *P* waves impinging.

Since the MASOX station is limited to just one three-component OBS, arrival-time technique cannot be used to triangulate the location of the events. After rotating the H1 and H2 components of the seismometer to the NS and EW directions as described in section 4.1, in order to determine direction of events origin a back azimuth (i.e., an angle of impinging seismic wave now measured clockwise from the geographic north) of each SDE was determined from the horizontal particle motion. As for earthquakes, such back azimuths

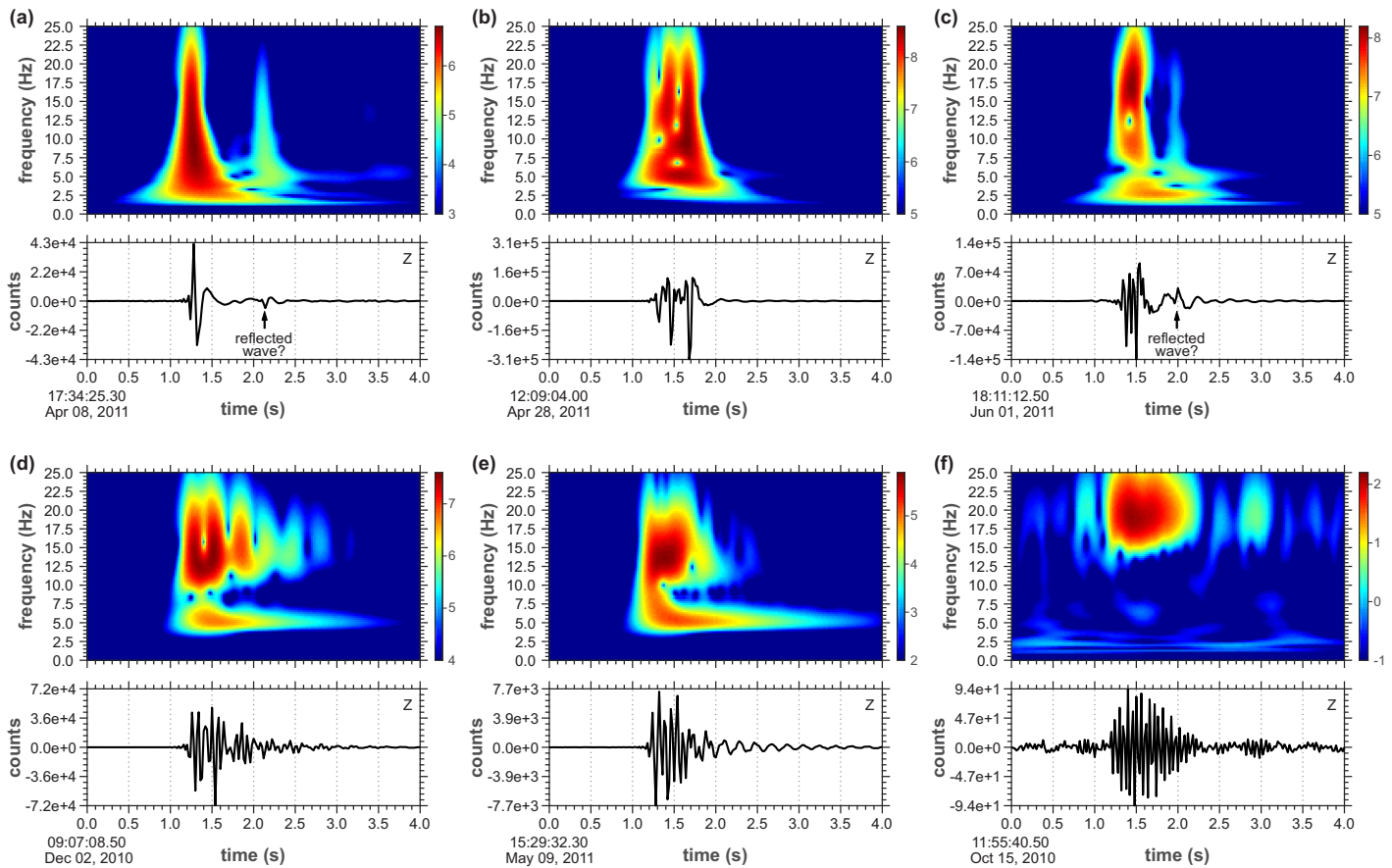


Figure 6. (a–f) Seismic records of vertical component Z of 6 SDEs identified by the STA/LTA algorithm and their spectrograms calculated by continuous wavelet transform using the Morlet wavelet. Colors of spectrograms are in $\log(\text{counts}^2/\text{Hz})$ units. Records were filtered with band-pass Butterworth filter in the frequency range 1.5–24 Hz. Arrows in Figures 6a and 6c indicate small amplitude waves, possible reflections from the sea surface, that are also clearly recognizable in the spectrograms.

can only be identified in the range 0–180° and polarity of the SDE’s first motion in the vertical plane is required to account for complete reconstruction of back azimuths. Visual inspection of several SDEs indicates that their onsets were equivocal in many cases and automatic identification of the first motion polarity cannot be reliably used. Thus, a 180° ambiguity of SDE back azimuths remains, which is significant in the assessment of the prevailing direction for the origin of sources. Nevertheless, constraining the orientation of events to 180° range does at least constrain the potential sources to an east-west direction.

4.3. High-Frequency Short Duration Events

Linear features are clearly apparent in the distribution of back azimuths from SDEs (Figure 7). They correspond to events with back azimuths across a wide range that changes progressively through time, as can be observed for the first 10 days in November 2010 as representative example (Figure 7b). Inspection of the seismograms of these events indicated that their waveforms, duration, and frequency content are remarkably similar to each other. They commonly reproduce the same high-frequency signal presented in Figure 6f.

To distinguish these high-frequency signals from other SDEs, a two-step automatic recognition procedure was applied. Since visual inspection reveals strong similarity between waveforms, a cross-correlation procedure against a well-defined master event—i.e., a representative event that contains all high-frequency SDEs—can be applied. However, minor shifts of position of the frequency peaks can cause misalignment of waveforms resulting in low cross-correlation coefficients. Instead, in the first step of automatic recognition we employed a cross correlation of amplitude envelopes to ensure the primary selection of events based on similar amplitude characteristics. The representative master event was chosen based on Figure 6f and the cross correlation was applied for each component of the seismic motion independently. Only events

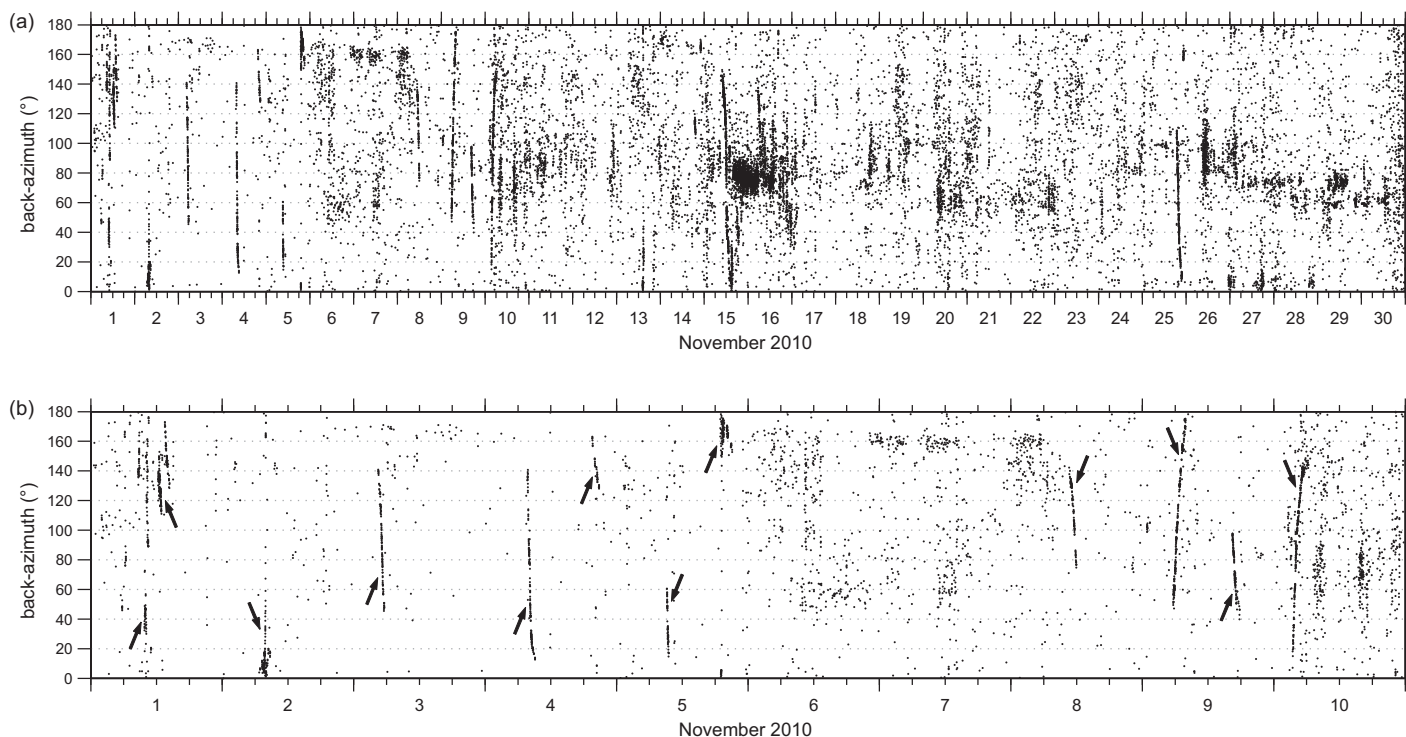


Figure 7. Distribution of back azimuths at times when the SDEs were identified by the STA/LTA algorithm. (a) Distribution of back azimuths during November 2010. (b) Distribution of back azimuths from 1 November to 10 November. Arrows indicate linear features in the distribution corresponding to HF-SDEs with waveforms resembling the signal shown in Figure 6f.

with a cross-correlation coefficients larger than 0.7 for at least two components were selected. In the second step, these preselected events were tested for the presence of a high-frequency peak using the following procedure: (1) The power spectrum smoothed by modified Daniell window with a length of 5 points (i.e., filtered by moving average window where the first and last points have half weight as the other points) was calculated for each component. (2) The maximum of the smoothed power spectrum within the 16–25 Hz frequency range (PSD_{max}) and the frequency at which this occurs (f_{max}) were determined. (3) The average value of the smoothed power spectrum, PSD_{avg} , in the frequency range 0–16 Hz was compared to PSD_{max} . A PSD_{max} at least 5 times larger than PSD_{avg} coupled with a rapid decrease of the smoothed power spectrum (less than 20% of PSD_{max} within 1 Hz), were the conditions to determine high-frequency peaks in the record (i.e., half-width of the frequency peak is less than 1 Hz). We classify events with high-frequency peaks on at least two components as high-frequency (HF-) SDEs.

HF-SDEs were abundant throughout the first 4 months from October 2010 to January 2011, but they are conspicuously missing from the remaining six months of the OBS deployment up until July, 2011. The HF-SDEs are grouped in irregularly occurring sequences lasting from tens of minutes to several hours (Figure 7). However, within every sequence their occurrence is fairly regular. The Schuster test (Ader & Avouac, 2013, and references therein) was used for a statistical analysis of the interevent times of occurrence (time between two successive HF-SDEs). In the test time of an event occurrence (t) relative to the investigated periodicity (T) is represented by phase angle $2\pi t/T$ of a phasor with unit amplitude. The vector sum of all phasors is considered as a 2-D walk for which a probability (p value) is evaluated under the hypothesis of random uniform distribution. Then value $1-p$ represents confidence level to discard the null hypothesis that events occurrence for considered period T have random distribution. The test calculates probabilities for a set of periods and thus gives a spectrum of Schuster p values—Schuster spectrum. The Schuster spectrum calculated for the HF-SDE occurrences manifests a strong probability above 99% confidence level for ~ 14 s periodic occurrence (Figure 8).

Progressive changes in source direction (e.g., on 9 November the back azimuths change from 60° to 180° over 2 h; Figure 7b), strong periodicity, and mutual similarity suggest generation from one or several

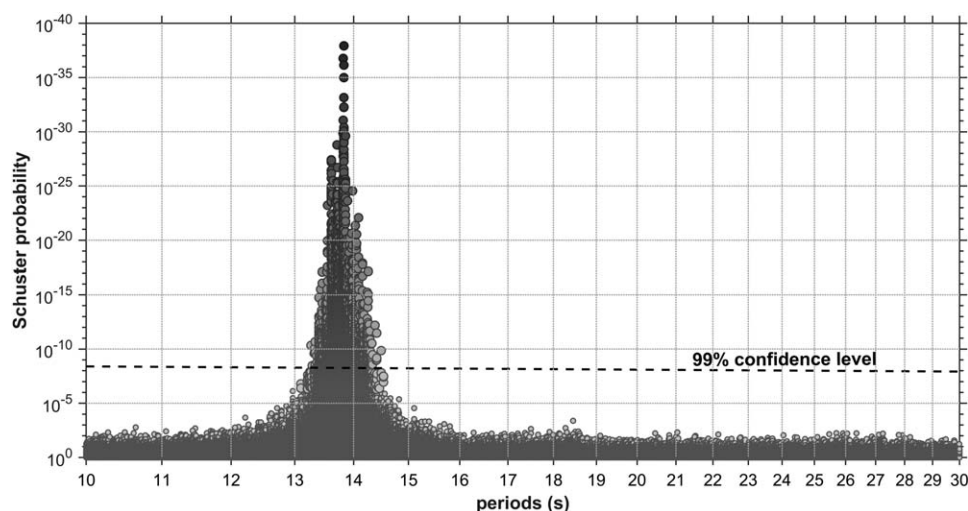


Figure 8. Schuster spectrum calculated for the occurrence of HF-SDEs. Probability at around 14 s period is above 99% confidence level to discard the null hypothesis that the occurrence of events is distributed randomly. Note the reversed orientation of y axis.

moving sources with similar mechanisms. An evenly distributed range of back azimuths through time reveals that the source appeared to traverse the OBS at steady speed and was probably located in seawater. A source located in the water column is consistent with the lack of *S* waves in the SDE records.

4.4. Location of SDE Sources

It is possible to estimate the location of the SDE sources if the distance as well as the direction of each event from the MASOX site can be constrained. Localized sources will express themselves in a distinct clustering in the distribution of back azimuths. Distinct clusters can be identified in the distribution of back azimuths of the SDEs for the 10 month operational period of the OBS (Figures 9 and 10). For example, on 15–16 November, a distinct cluster of back azimuths is centered at $\sim 80^\circ$, revealing a local SDE source over a relatively short-time period (hours to days). It is also noteworthy that in the first 5 months (October–February) of the OBS record many back azimuth clusters originate in the 60° to 120° ($\pm 180^\circ$) range, i.e., approximately from an east/west direction. Though, some of less intensive clusters of SDEs fall outside this range (e.g., from $\sim 160^\circ$ on 6–7 November) and on other days (e.g., 27–28 February and 8–9 July) the SDEs appear to originate from all possible directions. The latter are likely to be noise or the SDEs otherwise originating from a close, but broad source area. Such SDEs (i.e., SDEs with the back azimuths covering a wide range) predominantly occur in the latter 5 months (March–July) of the seismic record.

Due to their differing velocities and attenuation characteristics, the absence or presence of *S* waves as part of SDE signal package as well the duration of each SDE may be used to provide an estimate of the approximate distance to the source. If, for example, the *P* wave overlaps the *S* wave within a < 1 s, then a proximal source of the event can be inferred. Using *P* and *S* wave seismic velocities of ~ 1.5 – 2.4 km/s and ~ 0.3 – 0.5 km/s, respectively, for the upper 450 m of sediments nearby the MASOX site (Chabert et al., 2011), the distance to the SDE sources would have to be less than a few hundred meters. If *S* waves are absent, then SDEs from more distant sources are admissible, but under these circumstances the SDE waveforms may have a duration larger than 1 s due to dispersion and scattering. Nevertheless, SDEs from subseafloor sources of over $\sim 1,000$ m are unlikely to be recorded by the OBS since seismic energy will be strongly attenuated through marine fluid-saturated sediments (Chabert et al., 2011). Hence, we assume that the recorded SDEs have a source located within a 1,000 m of the MASOX site (black circle in Figure 2b).

The presence or absence of *S* waves in seismic records considerably depends on the source mechanism. In general, faulting sources (e.g., earthquakes) generate both *P* and *S* waves, but *S* waves are weak or entirely absent from volume sources like explosions or tension cracks (e.g., Aki & Richards, 2002). *S* waves are also usually absent in seismograms of long-period events and harmonic tremors that are recorded in volcanically active zones. These long-period events and harmonic tremors are associated with a resonance of fluid-filled

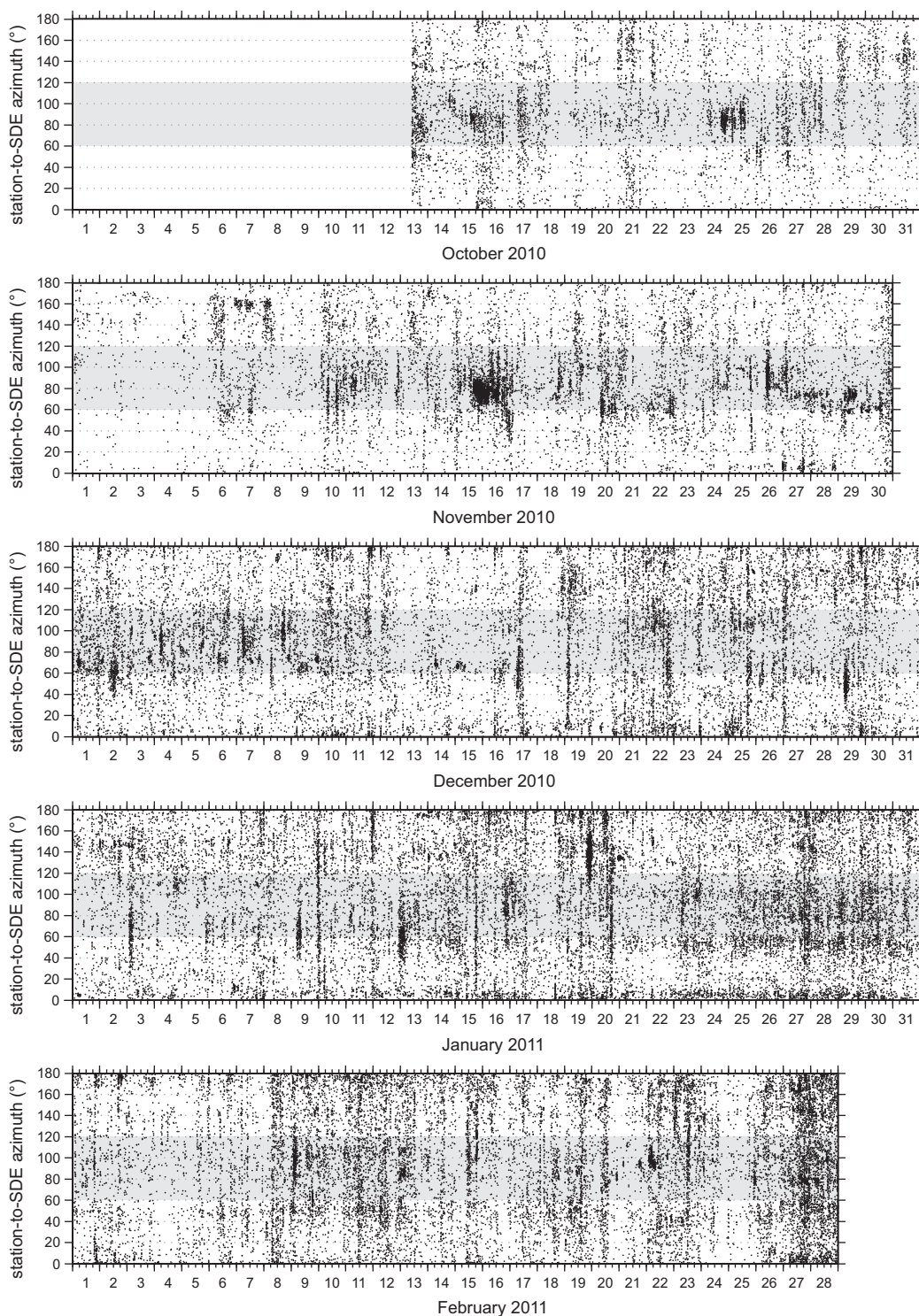


Figure 9. Distribution of back azimuths of the SDEs (station-to-SDE azimuth) for the first 5 months deployment period (October–February) of the OBS without HF-SDEs resembling the signal shown in Figure 6f. Shaded horizontal band indicates the back azimuth range 60–120°.

conduits or cavities when magma ascends toward the surface (e.g., Chouet, 1996). In addition, when the distance from a source is relatively small, i.e., less than or comparable to several wavelengths of radiated waves, near-field waves with significantly large amplitudes will render separation of *P* and *S* waves difficult (e.g., Aki & Richards, 2002).

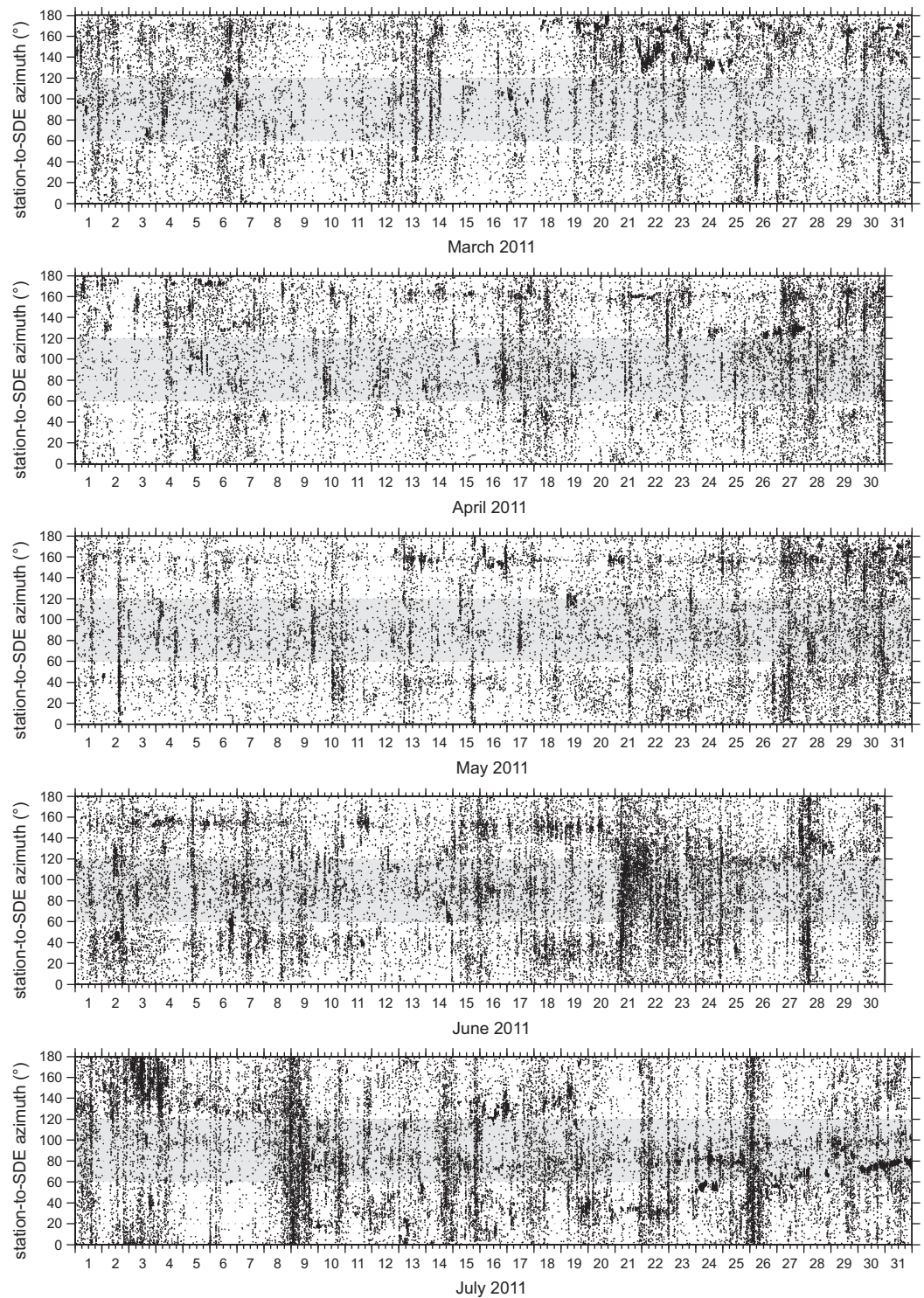


Figure 10. Distribution of back azimuths of the SDEs (station-to-SDE azimuth) for the second 5 months deployment period (March–July) of the OBS without HF-SDEs resembling the signal shown in Figure 6f. Shaded horizontal band indicates the back azimuth range 60–120°.

4.5. Variability of SDE Occurrence

The daily occurrence of identified SDEs is not uniformly distributed over time and varies considerably (black dashed line in Figure 11a). Smoothing the temporal distribution by a 10 day moving average filter (black

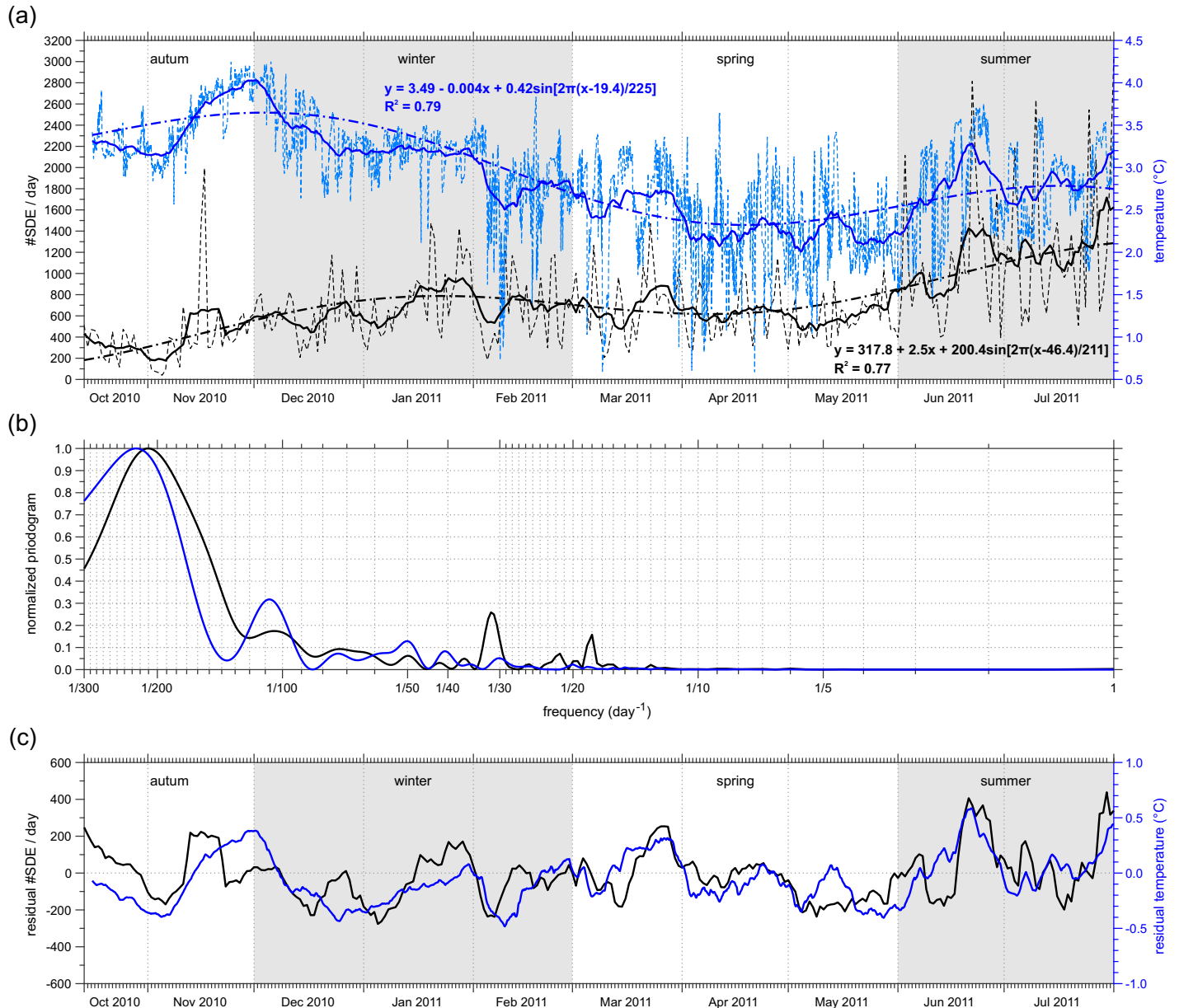


Figure 11. (a) Daily occurrence of the SDEs during the whole operational period of the OBS deployment (black dashed line) and bottom water temperature recorded 1.15 m above the seafloor at the MASOX location (blue dashed line) (Berndt et al., 2014). To highlight patterns in both distributions a 10 day moving average filter was applied (solid lines). Dash-dotted lines are least square fits to the smoothed distributions with fitting functions consisting of linear and sinusoidal part (see embedded relationships where x is time in days starting from 0 on 13 October 2010). For sinusoidal part periods of 211 and 225 days determined from periodograms were imposed. (b) Lomb-Scargle periodograms determined for smoothed daily occurrence of the SDEs and bottom water temperature after detrending by linear regression. Periodograms are normalized by their respective maximal values. (c) Residuals in daily occurrence of the SDEs and bottom water temperature after removing fitting functions from smoothed distributions. Both residuals are positively correlated at zero lag time ($R^2 = 0.6$, supporting information Figure S4) and manifest short-term variations in the smoothed time series.

solid line in Figure 11a) highlights general patterns in the data and suppresses fine-scale variations. A linear regression was applied on the smoothed distribution and showed increasing linear trend in the daily SDE occurrence from October 2010 to the end of July 2011. Subsequently, for the detrended smoothed distribution the Lomb-Scargle periodogram was determined and revealed a dominant period of 211 days in the time series and three other less significant periods at 18, 31, and 105 days (Figure 11b). In order to eliminate long-term variation (periodic part with period of 211 days) the smoothed distribution was fitted with a function consisting of the previously determined linear trend and a sinusoidal part with imposed period of 211

days (black dash-dotted line in Figure 11a). The final equation found by a least square method is well correlated with the smoothed signal ($R^2 = 0.77$). The fitting function is subtracted from the smoothed distribution retaining only short-term variations in the daily occurrence of SDEs (black line in Figure 11c).

Applying an analogous analysis to bottom water temperature variations (blue lines in Figure 11) recorded by a sensor located in the MASOX observatory provides a fitting function with a correlation coefficient of $R^2 = 0.79$. Smoothed temperature variations have a slight decreasing linear component and dominant sinusoidal part with a period of 225 days (Figures 11a and 11b). This sinusoidal part is phase shifted ~ 27 days before the dominant sinusoidal part determined for the SDE occurrence (see embedded equations for fitting functions and dash-dotted lines in Figure 11a). Comparing short-term variations of the SDEs and temperature results in a striking similarity (black versus blue line in Figure 11c). The residuals of each smoothed distribution have the highest positive correlation at zero lag time ($R^2 = 0.6$, supporting information Figure S4) despite few uncorrelated episodes (mid to end of November 2010, end of December 2010, and mid of May 2011) (Figure 11c).

Short-term variations in the SDE occurrence may raise the question about the effect of tides. Although identified periods of 18 and 31 days are close to long-period tidal constituents (14 and 28 days), they correspond to relatively narrow peaks in the periodograms and are therefore unlikely related. Moreover, a supplementary periodogram determined for hourly SDE and with other choice of moving average filter (24 h) does not indicate peaks at periods that could correspond to substantially stronger semidiurnal or diurnal tide (supporting information Figure S5). Although some episodes of high SDE occurrence appear to correspond to low tides (Figure 12a shows 11 days in January 2011 as an example), chi square test applied

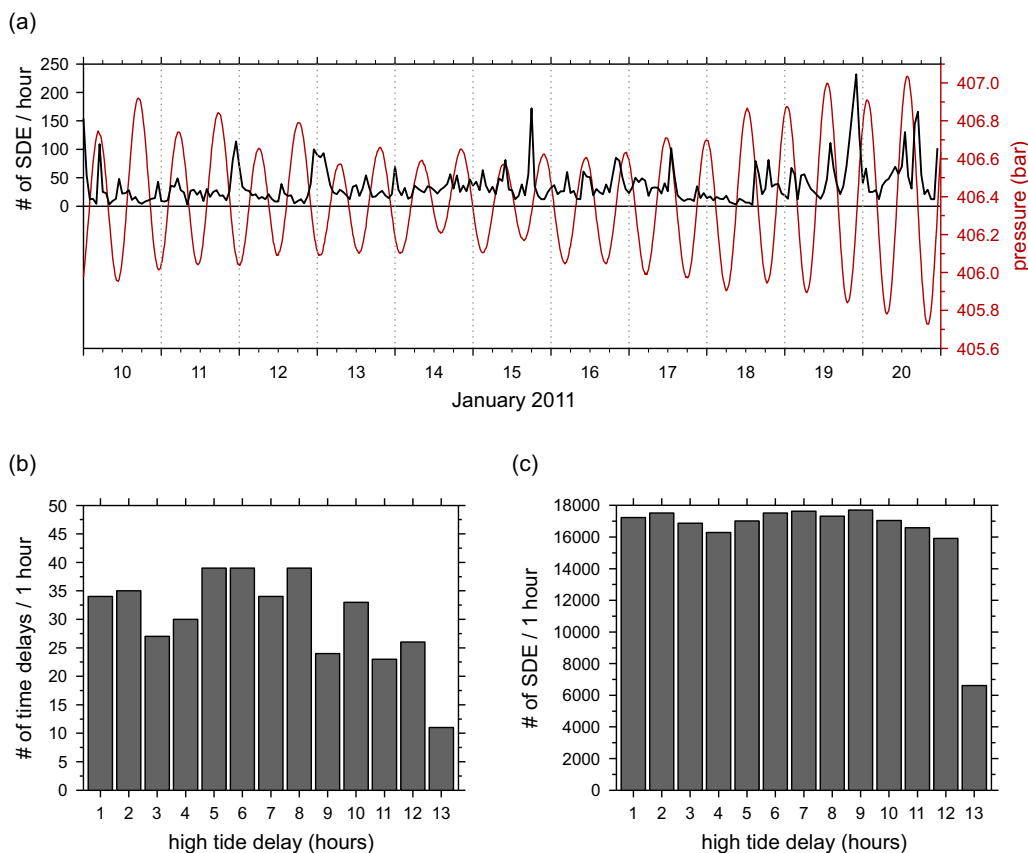


Figure 12. (a) Hourly number of the SDEs occurrence from 10 January to 20 January (black line) relative to tidal signal (red line) measured by the pressure sensor installed on the MASOX observatory. (b) Distribution of number of time delays calculated as the time difference between increased hourly number of the SDEs determined during the whole operational period of the OBS deployment and the nearest high tide that preceded this maximum. (c) Distribution of number of time delays calculated as the time difference between individual SDE occurrences and the nearest high tide that preceded this occurrence. Chi square tests of the distributions in Figures 12b and 12c showed no statistically significant difference from random distribution.

on time delays of peaks in the SDE occurrence after high tides (Figure 12b) does not testify any statistically significant difference from random distribution. Similarly, distribution of time delays of the individual SDE occurrences after high tides (Figure 12c) does not show any clear effect of tides either.

5. Discussion

5.1. Biological Origin of SDE

Large marine mammals (i.e., whales) generate acoustic signals that can be recorded by an OBS (e.g., McDonald et al., 1995; Rebull et al., 2006; Wilcock, 2012). Whales are abundant offshore west of Svalbard and it is likely that our OBS record contains signals from whales that call at frequencies comparable to the frequency range of the filtered seismograms (1.5–24 Hz). Blue whales (Mellinger & Clark, 2003) and humpback whales (e.g., Magnúsdóttir et al., 2015) recorded in the North Atlantic and in the subarctic waters of Iceland, respectively, can be ruled out as a source of SDEs or HF-SDEs. Their calls have either longer duration (2–5 s for blue whales) or show higher complexity and more structured sequences (humpback whales) that is not evident in the seismic data. Finback whales also emit low-frequency acoustic signals of which the so-called “20 Hz calls” from males are the most prominent (e.g., McDonald et al., 1995; Morano et al., 2012; Širović et al., 2004; Thompson et al., 1992). These calls are approximately 1 s in duration and consist of down-swept pulses from 40 to 15 Hz that center on ~20 Hz. Source level of the calls is between ~160 and ~190 dB re 1 μ Pa at 1 m (e.g., Watkins et al., 1987; Weirathmueller et al., 2013). They have been recorded in sequences of regular intercall intervals that vary between geographical regions (e.g., Thompson et al., 1992 reported 5, 9, and 18 s, McDonald et al., 1995, 19 s, Širović et al., 2004, ~13 and ~30 s, Rebull et al., 2006, 12–13 s, Morano et al., 2012, from 9.6 to 15.1 s) and in sequences that may last up to several days. The key characteristics of finback whale calls correspond very well to the HF-SDEs (supporting information Figures S6 and S7) which are characterized by a repeating pattern of short duration (<1 s) in sequences over several hours or days with a frequency peak that does indeed center on ~20 Hz. If considering distance of supposed moving sources of the HF-SDEs to be <1,000 m and based on progressive change in source direction (Figure 7b), the source speed would be <1 knot, which is consistent with reported unchanged vocalization of finback whales while remaining almost immobile for several hours (Rebull et al., 2006). Seasonal reproductive display and known migratory timing in finbacks behavior could explain the concentration of these signals in the seismic record during autumn and winter. Under the assumption that periodically occurring HF-SDEs do indeed originate from macrofauna (e.g., finback whales), they are herein disregarded for further considerations (Figures 9 and 10).

Characteristics of the remaining SDEs do not match those of other type of marine animals (e.g., fish). Seismic signals interpreted as fish bumps (i.e., due to interaction of marine animals with the seismometer) can have duration shorter than 1 s, but have a sharp, impulsive onset followed by a very regular amplitude decrease (see Figure 1 from Buskirk et al., 1981) and a spectrum with one or two very narrow frequency peaks (Buskirk et al., 1981). Their occurrence also has clear dependence on specific periods of the day (e.g., Boujard & Leatherland, 1992; Buskirk et al., 1981), a pattern that we neither observe in the data (Figure 13). Moreover,

we have recognized in the record several cases of strong SDE that were detected by both the seismometer and the hydrophone at the same time (Figure 14). Based on (1), the presence of small amplitude waves following some of the visually inspected SDEs after ~0.5–2 s (Figures 6a and 6c) that are interpreted as reflections from the sea surface, and (2) the detection of several signals on two separated instruments (i.e., the hydrophone and the seismometer) (Figure 14), we propose that the remaining SDEs are attributed to natural but nonbiological sources located at or below the seafloor.

5.2. Microearthquakes as a Source of the SDEs

The evolution of sedimentary basins of the western Svalbard margin has been strongly influenced by regional tectonics (e.g., Jokat et al., 2012) and postglacial flexural rebound (e.g., Landvik et al., 1998; Stewart et al., 2000). Numerous faults associated with the mid-ocean ridge rift systems outcrop on the bathymetry <50 km westward from the

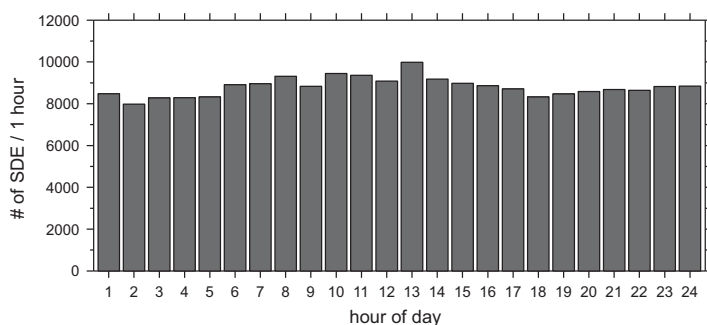


Figure 13. Hourly occurrence of the SDEs as a function of hour of the day. A slight increase in the SDEs occurrence at midday is noticeably, however, chi square test of the distribution showed no statistically significant difference from random distribution.

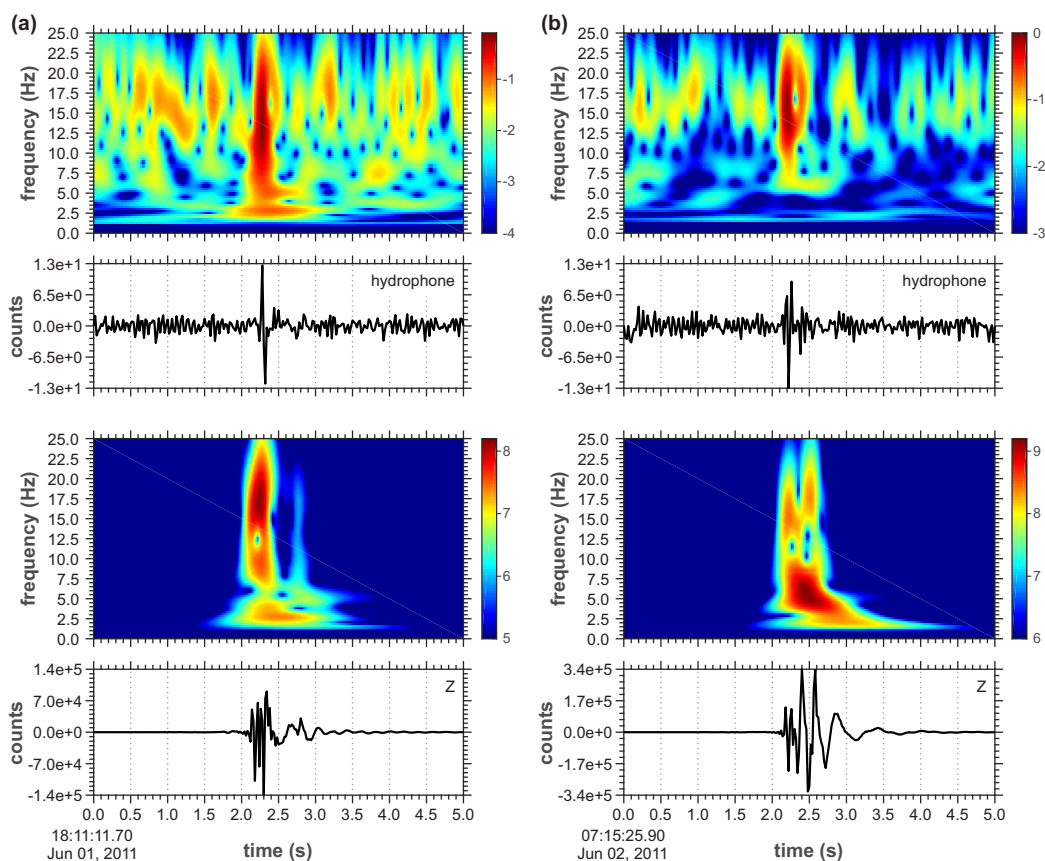


Figure 14. (a and b) Two short duration events recorded by the hydrophone and by the seismometer at the same time (only vertical component Z is shown). The SDE shown in Figure 14a is the same as in Figure 6c. Above every record is shown the corresponding spectrogram calculated by continuous wavelet transform with Morlet wavelet. Colors of spectrograms are in $\log(\text{counts}^2/\text{Hz})$ units. Records were filtered with band-pass Butterworth filter in the frequency range 1.5–24 Hz.

MASOX site (see Figure 1 from Vanneste et al., 2005). However, earthquakes originating from these faults can be ruled out since they have much longer duration than the observed SDEs—the closest earthquake with epicenter distance ~ 27 km, which occurred on 11 June 2011 (earthquake No. 247 in supporting information Table S1), clearly shows both *P* and *S* wave with ~ 8 s difference between arrival times (cf. Figure 3).

If recorded SDEs are earthquakes, they would have had to originate from faults in the vicinity of the MASOX site ($< 1,000$ m) in order to yield the overlapping of *P* and *S* waves. The occurrence of earthquakes implies active faulting, but no such activity has been documented in the Prins Karls Forland region. Nevertheless, we cannot entirely dismiss the possibility that part of SDEs are close weak earthquakes. The identified SDEs may thus document the microseismicity caused either by unrecognized faulting in the vicinity of the MASOX site or by other process(es) related to, for instance, fluid migration in the subsurface.

5.3. Gas Seepage and SubSeafloor Fluid Migration as a Source of the SDEs

Independent observations of thousands of acoustic gas flares offshore of Prins Karls Forland document extensive natural gas seepage from the seafloor across this region (Figures 1, 2a, and 2b) (e.g., Portnov et al., 2016; Sahling et al., 2014; Westbrook et al., 2009). In the absence of other mechanisms, and since the OBS is located within a well-known flare cluster (Figure 2b), it follows that the second—nonbiological—source of SDEs is related to processes of natural gas flow and release. We herein discuss the potential relationship between the nonbiological SDEs identified in the OBS record and fluid migration and associated seafloor gas seepage.

Opening and closing of subvertical cracks that are progressively in-filled by natural gas may lead to the generation of SDEs in a porous and saturated medium (Tary et al., 2012). Upward propagating gas filled cracks

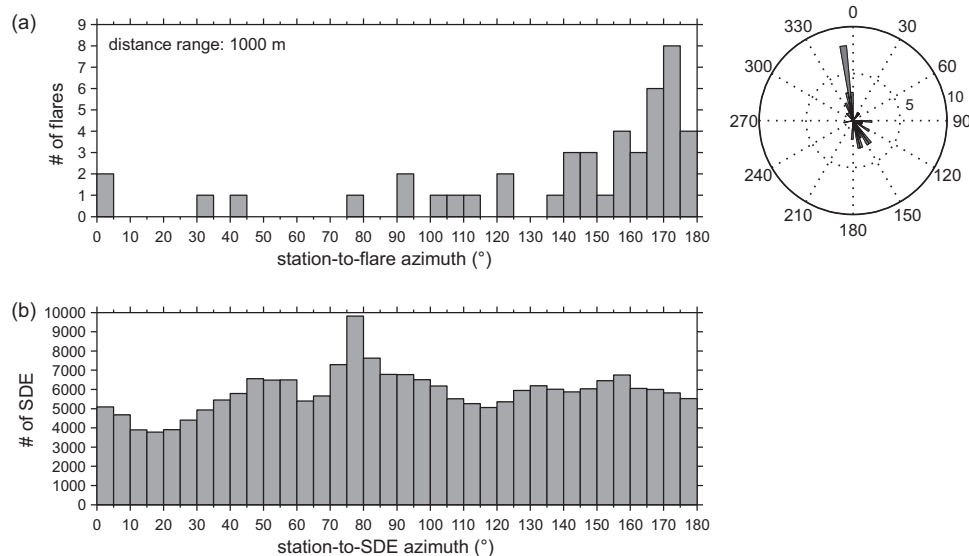


Figure 15. (a, left) Distribution of the station-to-flare azimuths determined from mapped locations of acoustic flares within 1,000 m distance range from the OBS site, recalculated for the azimuths 0–180°. (right) The same distribution of the station-to-flare azimuths shown in rose diagram for the azimuths 0–360°. (b) Distribution of the station-to-SDE azimuths.

can eventually attain the seafloor and trigger the release of gas to the water column. An SDE will be generated from the cracking itself or in conjunction with the ballistic expulsion of gas from the seafloor (e.g., Bons & van Milligen, 2001). Numerical modeling reveals that this mechanism yields seismic signals with a dominant frequency ~ 15 Hz (Tary et al., 2012) which is consistent with observations of SDEs related to fluid migration (e.g., Bayrakci et al., 2014; Sultan et al., 2011; Tary et al., 2012) and is within the frequency range (1.5–24 Hz) of the filtered seismograms recorded at the MASOX site.

Mapped locations of actual seepage sites (Figure 2b) can be compared with the origin directions of the SDEs (Figures 9 and 10). The maximum orientation of station-to-SDE azimuths (Figure 15b) falls between 70° and 85° indicating dominant east-west direction of SDE sources. However, the dominant orientation of the station-to-flare azimuths is $\sim 170^\circ$ (Figure 15a), i.e., the majority of mapped seep sites are located north-south within a 1,000 m radial zone centered at the MASOX site (Figure 2b). Thus, there is no clear agreement between the dominant azimuths of seep locations and the azimuths of the recorded SDEs. It may though indicate that the locations of seep sites varies both in time and space, and/or that there is additional seepage not recognized by conventional acoustic echo sounding techniques used to map gas flares. Recent measurements of dissolved methane in the water column west off Prins Karls Forland support the latter (J. Triest, personal communication, 2016).

High-resolution 2-D and 3-D seismic observations in the region document subseafloor fluid migration through vertical as well as lateral pathways (Rajan et al., 2012; Sarkar et al., 2012). This complex near-surface earth system involving fluid migration, seafloor seepage, and gas hydrate dynamics may suggest involving of several mechanisms generating SDEs. The interpretation of multiple mechanisms supports also the analysis of ocean tides on the SDE occurrence. Tidal modulation of gas discharge from gas reservoirs is well documented in a variety of environments (e.g., Algar et al., 2011; Bergès et al., 2015; Boles et al., 2001; Torres et al., 2002) where intensified gas release was observed during periods of low tide. Thus, missing clear effect of tides on the SDEs occurrence at the MASOX site (Figures 12b and 12c) indicate that besides gas seepage-related source mechanism of the SDEs another mechanism that is weakly influenced by tides is involved and perhaps more efficient in generating SDEs.

We hypothesize that the additional source of SDEs is an excitation of fluid-filled conduits as proposed by Díaz et al. (2007). The suggested mechanism is analogous to generating long-period events observed in volcanic areas (e.g., Chouet, 1996) based on the theoretical model of Chouet (1988). Long-period events with several distinct frequency peaks in the range 0.2–5 Hz are generated as resonance of fluid-filled cavities or

conduits excited by impulsive pressure transients (Chouet, 1988, 1996). Such long-period events have a similar seismic signature to the SDEs with a comparable frequency content and distinct lack of *S* wave arrivals. Successive occurrence of long-period events can eventually merge and form harmonic tremors as often recorded in volcanic provinces (e.g., Chouet & Matoza, 2013). We do not observe such tremors in the seismic record, however, their absence may result from different structural setting of the area as it is in volcanic areas. To confirm this presumption as well as generation of the SDE by a mechanism involving excitation of fluid-filled conduits requires further theoretical research and data from multiple instruments deployed at a test site.

5.4. Correlation of the SDE Occurrence With Temperature Variations

The analysis of temporal variations of the SDE occurrence (Figure 11) reveals short-term (\sim tens of days) as well as long-term (\sim 211 days) variation. On short-term scale these variations are positively correlated and having zero lag time with temperature fluctuations (supporting information Figure S4). Since the diffusion of temperature variations into the subseafloor is not immediate (e.g., Carslaw & Jaeger, 1959), bottom water temperature fluctuations as a controlling mechanism for short-term variations of the SDE occurrence can be ruled out.

Instead, we infer that fluid release fluctuations might affect bottom water temperature locally at the MASOX site and presumably be accompanied by changes in the number of SDE occurrences (Figure 11c) that are generated partially by gas seepage-related mechanism and partially by mechanism involving excitation of fluid-filled pathways. In the region of the western Svalbard margin, data from active seismic experiments are collected yearly by the University of Tromsø on board R/V Helmer Hanssen using the P-Cable streamers (e.g., Petersen et al., 2010; Planke et al., 2009) that can be configured for 2-D or 3-D high-resolution seismic acquisition (ca. 6 and 5 m lateral and vertical resolution, respectively). A NE-SW oriented 2-D seismic transect collected over the MASOX site shows patchy high amplitude, reverse polarity areas that suggest accumulation of fluids up-dip along a reflector (i.e., perhaps stratigraphic or possibly a gas hydrate-related bottom simulating reflector) that extends toward the active seafloor seepage region (Figure 2c). Localized high RMS amplitudes on high-resolution 3-D seismic data provide another supporting evidence for the presence of shallow fluid accumulations nearby the MASOX site (Figure 2b). From these shallow accumulations fluids may be episodically released and subsequently increase bottom water temperatures. Transient fluctuations in intensity of fluid flux from the seafloor have also been shown in other margins to alter bottom water temperatures locally (e.g., Momma et al., 1998). Thus, we postulate that the short-term variations may reflect transient fluctuation in the flux of warmer fluids released from the seafloor. However, additional data on fluid release and temperature measurements in sediments and bottom water are needed to confirm this hypothesis. If the coupling of short-term variations between temperature and the SDE occurrence is real, our observation may have important implications for understanding the mechanisms controlling the release of gas from the seafloor. Variations in the regional stresses or the pore fluid pressure controlling fluid dynamics would be constrained to periods of tens of days.

Long-term variation of the SDE occurrence and bottom water temperature is more difficult to reconcile (Figures 11a and 11b). Identification of linear trends and periods of 211 and 225 days of the SDE occurrence and bottom water temperature, respectively, might not be sufficiently constrained by the 10 month (297 days) long time series. Rather, they may be a part of seasonal oscillation as documented by Berndt et al. (2014) for 2 years measurement of bottom water temperature at the MASOX site. We speculate that the long-term variation in the number of recorded SDEs may be related to the dynamics of the gas hydrate system. Since the MASOX site falls just within the upper pinch-out of the gas hydrate stability zone (Figure 2) (Westbrook et al., 2009), here the stability of shallow gas hydrates is assumed to be highly sensitive to regional changes in bottom water temperature (Berndt et al., 2014; Westbrook et al., 2009) as determined by bottom currents (Cottier et al., 2007). Seasonal bottom water temperature changes affect the temperature of the upper few meters of sediments with time delay (e.g., Carslaw & Jaeger, 1959) and eventually may dissociate gas hydrates, if present. The delay of \sim 27 days between dominant sinusoidal parts in the SDE occurrence and bottom water temperature (Figure 11a) might therefore be caused by a feedback of gas hydrate and associated seepage system to seasonal temperature change. However, shallow gas hydrates have not yet been retrieved in the area at the same water depth as the MASOX observatory, thought they are commonly assumed to be present in the region off Prins Karls Forland (e.g., Berndt et al., 2014; Chabert et al., 2011; Rajan et al., 2012; Sarkar et al., 2012; Westbrook et al., 2009). Therefore, we cannot

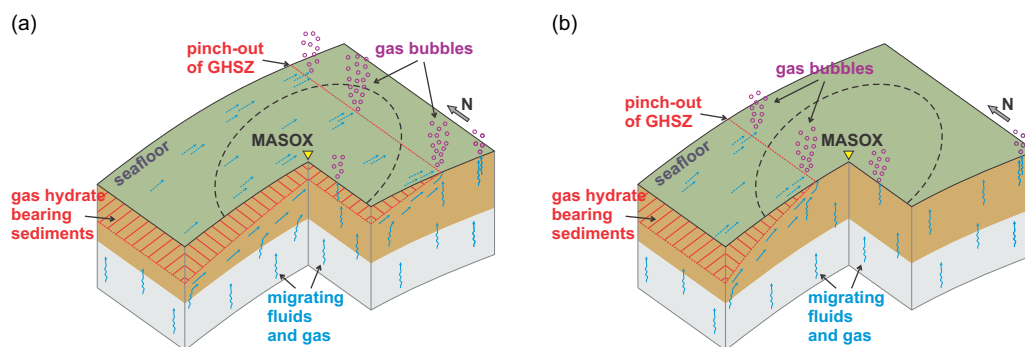


Figure 16. Schematic model illustrating vertical and lateral fluid migration and gas release at the MASOX site. Dashed black line represents inferred detectability range of the OBS. (a) At large extent of assumed gas hydrate stability zone (GHSZ) lateral migration below the OBS is enhanced and SDEs originating from numerous sources (mainly lateral migration pathways) and from a wide azimuth range can be detected. (b) When shallow gas hydrates have smaller extent, more significant source of SDEs within detectability range of the OBS is gas seepage through vertical veins and fractures that are projected within more discrete and narrow zones.

firmly conclude with an explanation for the delay between long-term variation of the SDE occurrence and bottom water temperature.

Conceptually, we envision that the zone of maximum concentration of seepage sites might be controlled by the seasonal variation of the extent of gas hydrate stability zone (Berndt et al., 2014; Westbrook et al., 2009), which experiences a spatial shift in the east-west direction (Figure 16). The SDEs have a larger spatial distribution when they are caused by excitation in lateral fluid migration pathways. When projected to the surface, multiple SDE sources occur inside these lateral migration paths and appear horizontally distributed (Figure 16a). On the other hand, focused seafloor seepage through vertical veins and fractures would project within more discrete and narrow zones (Figure 16b). However, the occurrence of seepage-related SDEs overlap with the occurrence of SDEs related to vibration of fluid migration pathways throughout the OBS operational period and it is hence difficult to separate them reliably, which is even more complicated given the data from one seismometer.

6. Conclusions

From October 2010 to August 2011, an OBS was deployed as part of the MASOX observatory at 389 m water depth on the upper continental slope offshore western Svalbard. The vicinity is characterized by abundant natural gas present in subseafloor sediments and numerous gas flares observed in the water column. The OBS successfully recorded continuous microseismic activity over a 297 day operational period. The analysis leads to the following key findings and hypotheses:

1. Almost 300 earthquakes are identified in the OBS record that are associated with known earthquakes located by the International Seismic Center and NORSAR. Polarization analysis of earthquake generated *P* waves enables the reliable and unambiguous determination of the correct orientation of horizontal components of the seismometer.
2. In addition to the earthquakes recorded by the OBS, we identified 220,000 SDEs which have a duration of less than 1 s. While part of these events have signatures clearly corresponding to finback whale calls, a large number of events are natural but nonbiological. We hypothesize two main source mechanisms for this second type of SDEs—fracturing processes related to seafloor gas seepage and vibration of subseafloor fluid migration pathways. Fault-related microseismicity in close proximity to the MASOX observatory cannot be completely discounted.
3. The occurrence of the second type of SDEs varies on both short-term (~tens of days) and seasonal (on the order of several months) time scales. The short-term variations are positively correlated with transient variations in bottom water temperature. We presume a relation to the local gas hydrate dynamics driven by changes in bottom water temperature controlled by regional currents.

The analysis of SDEs documents for the first time microseismic activity associated with fluid migration and seafloor seepage offshore the western Svalbard continental margin. Our study validates a new approach

based on microseismic monitoring for constraining the mechanisms that control fluid dynamics in the near-surface sediment.

Acknowledgments

This research is part of the Centre for Arctic Gas Hydrate, Environment and Climate. It was supported by the Research Council of Norway through its Centres of Excellence funding scheme, grant 223259. We are grateful to the crews and scientific parties of all MASOX-related cruises (R/V Jan Mayen, R/V S. James Clark Ross, F/S Maria S. Merian) for their assistance and special thanks are extended to the submersible JAGO team Jürgen Schauer (GEOMAR, Germany) and Veit Huehnerbach (GEOMAR, Germany) for recovering the OBS. We thank Christian Berndt (GEOMAR, Germany) for helpful suggestions and comments that improved the manuscript as well as Monica Winsborrow (CAGE, Norway) for assistance with proof reading the text. We also thank the anonymous reviewers for their valuable comments that substantially improved final quality of the manuscript. Supporting information Figure S6b is reprinted with permission from Simon et al. (2010), Singing behavior of fin whales in the Davis Strait with implications for mating, migration, and foraging, *J. Acoust. Soc. Am.*, 128, 3200–3210. Copyright 2010, Acoustic Society of America. Supporting information Figure S7c is reprinted with permission from Rebull et al. (2006), Tracking fin whale calls offshore the Galicia Margin, North East Atlantic Ocean, *J. Acoust. Soc. Am.*, 120, 2077–2085. Copyright 2006, Acoustic Society of America. Earthquakes data are available from the Reviewed Bulletin of the International Seismic Center (<http://www.isc.ac.uk>) and from the NORRAR regional reviewed bulletin (<http://www.norsardata.no/NDC/bulletins/regional>). The OBS seismic records are available by contacting the authors at peter.franek@uit.no, jurgen.mienert@uit.no or stefan.buenz@uit.no.

References

- Addison, P. S. (2002). *The illustrated wavelet transform handbook—Introductory theory and applications in science, engineering, medicine and finance*. Bristol, UK: Institute of Physics Publishing.
- Ader, T. J., & Avouac, J.-P. (2013). Detecting periodicities and declustering in earthquake catalogs using the Schuster spectrum, application to Himalayan seismicity. *Earth and Planetary Science Letters*, 377–378, 97–105. <https://doi.org/10.1016/j.epsl.2013.06.032>
- Aki, K., & Richards, P. G. (2002). *Quantitative seismology* (2nd ed.). Sausalito, CA: University Science Books.
- Albarello, D., Palo, M., & Martinelli, G. (2012). Monitoring methane emission of mud volcanoes by seismic tremor measurements: A pilot study. *Natural Hazards and Earth System Sciences*, 12, 3617–3629. <https://doi.org/10.5194/nhess-12-3617-2012>
- Algar, C. K., Boudreau, B. P., & Barry, M. A. (2011). Release of multiple bubbles from cohesive sediments. *Geophysical Research Letters*, 38, L08606. <https://doi.org/10.1029/2011GL046870>
- Allen, R. V. (1978). Automatic earthquake recognition and timing from single traces. *Bulletin of the Seismological Society of America*, 68, 1521–1532.
- Auriac, A., Whitehouse, P. L., Bentley, M. J., Patton, H., Lloyd, J. M., & Hubbard, A. (2016). Glacial isostatic adjustment associated with the Barents Sea ice sheet: A modelling inter-comparison. *Quaternary Science Reviews*, 147, 122–135. <https://doi.org/10.1016/j.quascirev.2016.02.011>
- Baer, M., & Kradolfer, U. (1987). An automatic phase picker for local and teleseismic events. *Bulletin of the Seismological Society of America*, 77, 1437–1445.
- Bayrakci, G., Scalabrin, C., Dupré, S., Leblond, I., Tary, J.-B., Lanteri, N., . . . Géli, L. (2014). Acoustic monitoring of gas emissions from the seafloor. Part II: A case study from the Sea of Marmara. *Marine Geophysical Research*, 35, 211–229. <https://doi.org/10.1007/s11001-014-9227-7>
- Bergès, B. J. P., Leighton, T. G., & White, P. R. (2015). Passive acoustic quantification of gas fluxes during controlled gas release experiments. *International Journal of Greenhouse Gas Control*, 38, 64–79. <https://doi.org/10.1016/j.ijggc.2015.02.008>
- Berndt, C., Feseker, T., Treude, T., Krastel, S., Liebetrau, V., Niemann, H., . . . Steinle, L. (2014). Temporal constraints on hydrate-controlled methane seepage off Svalbard. *Science*, 343, 284–287. <https://doi.org/10.1126/science.1246298>
- Biaostoch, A., Treude, T., Rüpke, L. H., Riebesell, U., Roth, C., Burwicz, E. B., . . . Wallmann, K. (2011). Rising Arctic Ocean temperatures cause gas hydrate destabilization and ocean acidification. *Geophysical Research Letters*, 38, L08602. <https://doi.org/10.1029/2011GL047222>
- Boles, J. R., Clark, J. F., Leifer, I., & Washburn, L. (2001). Temporal variation in natural methane seep rate due to tides, Coal Oil Point area, California. *Journal of Geophysical Research*, 106, 27077–27086. <https://doi.org/10.1029/2000JC000774>
- Bons, P. D., & van Milligen, B. P. (2001). New experiment to model self-organized critical transport and accumulation of melt and hydrocarbons from their source rocks. *Geology*, 29, 919–922. [https://doi.org/10.1130/0091-7613\(2001\)029<0919:NETMSO>2.0.CO;2](https://doi.org/10.1130/0091-7613(2001)029<0919:NETMSO>2.0.CO;2)
- Boujard, T., & Leatherland, J. F. (1992). Circadian rhythms and feeding time in fishes. *Environmental Biology of Fishes*, 35, 109–131. <https://doi.org/10.1007/BF00002186>
- Buskirk, R. E., Frohlich, C., Latham, G. V., Chen, A. T., & Lawton, J. (1981). Evidence that biological activity affects Ocean Bottom Seismograph recordings. *Marine Geophysical Research*, 5, 189–205.
- Carlslaw, H. S., & Jaeger, J. C. (1959). *Conduction of heat in solids* (2nd ed.). Oxford, UK: Clarendon Press.
- Chabert, A., Minshull, T. A., Westbrook, G. K., Berndt, C., Thatcher, K. E., & Sarkar, S. (2011). Characterization of a stratigraphically constrained gas hydrate system along the western continental margin of Svalbard from ocean bottom seismometer data. *Journal of Geophysical Research*, 116, B12102. <https://doi.org/10.1029/2011JB008211>
- Chouet, B. (1988). Resonance of a fluid-driven crack: Radiation properties and implications for the source of long-period events and harmonic tremor. *Journal of Geophysical Research*, 93, 4375–4400. <https://doi.org/10.1029/JB093iB05p04375>
- Chouet, B. A. (1996). Long-period volcano seismicity: Its source and use in eruption forecasting. *Nature*, 380, 309–316. <https://doi.org/10.1038/380309a0>
- Chouet, B. A., & Matoza, R. S. (2013). A multi-decadal view of seismic methods for detecting precursors of magma movement and eruption. *Journal of Volcanology and Geothermal Research*, 252, 108–175. <https://doi.org/10.1016/j.jvolgeores.2012.11.013>
- Cottier, F. R., Niilsen, F., Inall, M. E., Gerland, S., Tverberg, V., & Svendsen, H. (2007). Wintertime warming of an Arctic shelf in response to large-scale atmospheric circulation. *Geophysical Research Letters*, 34, L10607. <https://doi.org/10.1029/2007GL029948>
- Crane, K., Doss, H., Vogt, P., Sundvor, E., Cherkashov, G., Poroshina, I., & Joseph, D. (2001). The role of the Spitsbergen shear zone in determining morphology, segmentation and evolution of the Knipovich Ridge. *Marine Geophysical Research*, 22, 153–205. <https://doi.org/10.1023/A:1012288309435>
- Crotwell, H. P., Owens, T. J., & Ritsema, J. (1999). The TauP Toolkit: Flexible seismic travel-time and ray-path utilities. *Seismological Research Letters*, 70, 154–160. <https://doi.org/10.1785/gssrl.70.2.154>
- Dehls, J. F., Olesen, O., Bungum, H., Hicks, E. C., Lindholm, C. D., & Riis, F. (2000). *Neotectonic map: Norway and adjacent areas*. Trondheim, Norway: Geological Survey of Norway.
- Díaz, J., Gallart, J., & Gaspà, O. (2007). Atypical seismic signals at the Galicia Margin, North Atlantic Ocean, related to the resonance of sub-surface fluid-filled cracks. *Tectonophysics*, 433, 1–13. <https://doi.org/10.1016/j.tecto.2007.01.004>
- Dickens, G. R. (2003). Rethinking the global carbon cycle with a large, dynamic and microbially mediated gas hydrate capacitor. *Earth and Planetary Science Letters*, 213, 169–183. [https://doi.org/10.1016/S0012-821X\(03\)00325-X](https://doi.org/10.1016/S0012-821X(03)00325-X)
- Earle, P. S., & Shearer, P. M. (1994). Characterization of global seismograms using an automatic-picking algorithm. *Bulletin of the Seismological Society of America*, 84, 366–376.
- Eldholm, O., Faleide, J. I., & Myhre, A. M. (1987). Continent-ocean transition at the western Barents Sea/Svalbard continental margin. *Geology*, 15, 1118–1122. [https://doi.org/10.1130/0091-7613\(1987\)15<1118:CTATWB>2.0.CO;2](https://doi.org/10.1130/0091-7613(1987)15<1118:CTATWB>2.0.CO;2)
- Embricco, D., Marinaro, G., Frugoni, F., Monna, S., Etiope, G., Gasperini, L., . . . Favali, P. (2014). Monitoring of gas and seismic energy release by multiparametric benthic observatory along the North Anatolian Fault in the Sea of Marmara (NW Turkey). *Geophysical Journal International*, 196, 850–866. <https://doi.org/10.1093/gji/ggt436>
- Engen, Ø., Eldholm, O., & Bungum, H. (2003). The Arctic plate boundary. *Journal of Geophysical Research*, 108, 2075. <https://doi.org/10.1029/2002JB001809>
- Faleide, J. I., Vågnes, E., E., & Gudlaugsson, S. T. (1993). Late Mesozoic-Cenozoic evolution of the south-western Barents Sea in a regional rift-shear tectonic setting. *Marine and Petroleum Geology*, 10, 186–214. [https://doi.org/10.1016/0264-8172\(93\)90104-Z](https://doi.org/10.1016/0264-8172(93)90104-Z)

- Ferré, B., Mienert, J., & Feseker, T. (2012). Ocean temperature variability for the past 60 years on the Norwegian-Svalbard margin influences gas hydrate stability on human time scales. *Journal of Geophysical Research*, *117*, C10017. <https://doi.org/10.1029/2012JC008300>
- Franeck, P., Mienert, J., Buenz, S., & Géli, L. (2014). Character of seismic motion at a location of a gas hydrate-bearing mud volcano on the SW Barents Sea margin. *Journal of Geophysical Research: Solid Earth*, *119*, 6159–6177. <https://doi.org/10.1002/2014JB010990>
- Gentz, T., Damma, E., Schneider von Deimling, J., Mau, S., McGinnis, D. F., & Schlüter, M. (2014). A water column study of methane around gas flares located at the West Spitsbergen continental margin. *Continental Shelf Research*, *72*, 107–118. <https://doi.org/10.1016/j.csr.2013.07.013>
- Graves, C. A., Steinle, L., Rehder, G., Niemann, H., Connelly, D. P., Lowry, D., . . . James, R. H. (2015). Fluxes and fate of dissolved methane released at the seafloor at the landward limit of the gas hydrate stability zone offshore western Svalbard. *Journal of Geophysical Research: Oceans*, *120*, 6185–6201. <https://doi.org/10.1002/2015JC011084>
- Ingólfsson, Ó., & Landvik, J. Y. (2013). The Svalbard-Barents Sea ice-sheet—Historical, current and future perspectives. *Quaternary Science Reviews*, *64*, 33–60. <https://doi.org/10.1016/j.quascirev.2012.11.034>
- Isaksen, I. S. A., Gauss, M., Myhre, G., Walter Anthony, K. M., & Ruppel, C. (2011). Strong atmospheric chemistry feedback to climate warming from Arctic methane emissions. *Global Biogeochemical Cycles*, *25*, GB2002. <https://doi.org/10.1029/2010GB003845>
- Jokat, W., Kollofrath, J., Geissler, W. H., & Jensen, L. (2012). Crustal thickness and earthquake distribution south of the Logachev Seamount, Knipovich Ridge. *Geophysical Research Letters*, *39*, L08302. <https://doi.org/10.1029/2012GL051199>
- Johnston, A. C. (1989). The effect of large ice sheets on earthquake genesis. In S. Gregersen & P. W. Basham (Eds.), *Earthquakes at North-Atlantic passive margins: Neotectonics and postglacial rebound* (pp. 581–599). Dordrecht, the Netherlands: Kluwer.
- Jurkevics, A. (1988). Polarization analysis of three-component array data. *Bulletin of the Seismological Society of America*, *78*, 1725–1743.
- Kennett, B. L. N., Engdahl, E. R., & Buland, R. (1995). Constraints on seismic velocities in the Earth from travel times. *Geophysical Journal International*, *122*, 108–124. <https://doi.org/10.1111/j.1365-246X.1995.tb03540.x>
- Landvik, J. Y., Bondevik, S., Elverhøi, A., Fjeldskaar, W., Mangerud, J., Salvigsen, O., . . . Vorren, T. O. (1998). The last glacial maximum of the Barents Sea and Svalbard area: Ice sheet extent and configuration. *Quaternary Science Reviews*, *17*, 43–75. [https://doi.org/10.1016/S0277-3791\(97\)00066-8](https://doi.org/10.1016/S0277-3791(97)00066-8)
- Landvik, J. Y., Ingólfsson, Ó., Mienert, J., Lehman, S. J., Solheim, A., Elverhøi, A., & Ottesen, D. (2005). Rethinking Late Weichselian ice-sheet dynamics in coastal NW Svalbard. *Boreas*, *34*, 7–24. <https://doi.org/10.1111/j.1502-3885.2005.tb01001.x>
- Magnúsdóttir, E. E., Miller, P. J. O., Lim, R., Rasmussen, M. H., Lammers, M. O., & Svavarsson, J. (2015). Humpback whale (*Megaptera novaeangliae*) song unit and phrase repertoire progression on a subarctic feeding ground. *Journal of the Acoustical Society of America*, *138*, 3362–3374. <https://doi.org/10.1121/1.4935517>
- McDonald, M. A., Hildebrand, J. A., & Webb, S. C. (1995). Blue and fin whales observed on a seafloor array in the Northeast Pacific. *Journal of the Acoustical Society of America*, *98*, 712–721. <https://doi.org/10.1121/1.413565>
- Mellinger, D. K., & Clark, C. W. (2003). Blue whale (*Balaenoptera musculus*) sounds from the North Atlantic. *Journal of the Acoustical Society of America*, *114*, 1108–1119. <https://doi.org/10.1121/1.1593066>
- Momma, H., Iwase, R., Mitsuzawa, K., Kaiho, Y., & Fujiwara, Y. (1998). Preliminary results of a three-year continuous observation by a deep seafloor observatory in Sagami Bay, central Japan. *Physics of the Earth and Planetary Interiors*, *108*, 263–274. [https://doi.org/10.1016/S0031-9201\(98\)00107-1](https://doi.org/10.1016/S0031-9201(98)00107-1)
- Montalbetti, J. F., & Kanasevich, E. R. (1970). Enhancement of teleseismic body phases with a polarization filter. *Geophysical Journal of the Royal Astronomical Society*, *21*, 119–129. <https://doi.org/10.1111/j.1365-246X.1970.tb01771.x>
- Morano, J. L., Salisbury, D. P., Rice, A. N., Conklin, K. L., Falk, K. L., & Clark, C. W. (2012). Seasonal and geographical patterns of fin whale song in the western North Atlantic Ocean. *Journal of the Acoustical Society of America*, *132*, 1207–1212. <https://doi.org/10.1121/1.4730890>
- Mosar, J., Eide, E. A., Osmundsen, P. T., Sommaruga, A., & Torsvik, T. H. (2002). Greenland–Norway separation: A geodynamic model for the North Atlantic. *Norwegian Journal of Geology*, *82*, 281–298.
- Osler, J., & Chapman, D. M. F. (1998). Quantifying the interaction of an ocean bottom seismometer with the seabed. *Journal of Geophysical Research*, *103*, 9879–9894. <https://doi.org/10.1029/98JB00392>
- Ottesen, D., Dowdeswell, J. A., & Rise, L. (2005). Submarine landforms and the reconstruction of fast-flowing ice streams within a large Quaternary ice sheet: The 2500-km-long Norwegian-Svalbard margin (57°–80°N). *Bulletin of the Geological Society of America*, *117*, 1033–1050. <https://doi.org/10.1130/B25577.1>
- Patton, H., Andreassen, K., Bjarnadóttir, L. R., Dowdeswell, J. A., Winsborrow, M. C. M., Noormets, R., . . . Hubbard, A. (2015). Geophysical constraints on the dynamics and retreat of the Barents Sea ice sheet as a paleobenchmark for models of marine ice sheet deglaciation. *Reviews of Geophysics*, *53*, 1051–1098. <https://doi.org/10.1002/2015RG000495>
- Peive, A. A., & Chamov, N. P. (2008). Basic tectonic features of the Knipovich Ridge (North Atlantic) and its neo-tectonic evolution. *Geotectonics*, *42*, 31–47. <https://doi.org/10.1134/S0016852108010044>
- Person, R., Favali, P., Ruhl, H. A., Beranzoli, L., Rolin, J.-F., Waldmann, C., . . . Thomsen, L. (2015). From ESONET multidisciplinary scientific community to EMSO novel European research infrastructure for ocean observation. In P. Favali, L. Baranzoli, & A. De Santis (Eds.), *Seafloor observatories: A new vision of the Earth from the Abyss* (pp. 531–563). Berlin, Germany: Springer. <https://doi.org/10.1007/978-3-642-11374-1>
- Petersen, C. J., Bünz, S., Hustoft, S., Mienert, J., & Klaeschen, D. (2010). High-resolution P-Cable 3D seismic imaging of gas chimney structures in gas hydrated sediments of an Arctic sediment drift. *Marine and Petroleum Geology*, *27*, 1981–1994. <https://doi.org/10.1016/j.marpetgeo.2010.06.006>
- Planke, S., Eriksen, F. N., Berndt, C., Mienert, J., & Masson, D. (2009). Spotlight on technology: P-Cable high-resolution seismic. *Oceanography*, *22*, 85. <https://doi.org/10.5670/oceanog.2009.09>
- Plaza-Faverola, A., Bünz, S., Johnson, J. E., Chand, S., Knies, J., Mienert, J., & Franeck, P. (2015). Role of tectonic stress in seepage evolution along the gas hydrate-charged Vestnesa Ridge, Fram Strait. *Geophysical Research Letters*, *42*, 733–742. <https://doi.org/10.1002/2014GL062474>
- Pohlman, J. W., Bauer, J. E., Waite, W. F., Osburn, C. L., & Chapman, N. R. (2011). Methane hydrate-bearing seeps as a source of aged dissolved organic carbon to the oceans. *Nature Geoscience*, *4*, 37–41. <https://doi.org/10.1038/ngeo1016>
- Portnov, A., Vadakkepuliambatta, S., Mienert, J., & Hubbard, A. (2016). Ice-sheet-driven methane storage and release in the Arctic. *Nature Communications*, *7*, 10314. <https://doi.org/10.1038/ncomms10314>
- Rajan, A., Mienert, J., & Bünz, S. (2012). Acoustic evidence for a gas migration and release system in Arctic glaciated continental margins offshore NW-Svalbard. *Marine and Petroleum Geology*, *32*, 36–49. <https://doi.org/10.1016/j.marpetgeo.2011.12.008>
- Rebull, O. G., Cusi, J. D., Fernández, M. R., & Muset, J. G. (2006). Tracking fin whale calls offshore the Galicia Margin, North East Atlantic Ocean. *Journal of the Acoustical Society of America*, *120*, 2077–2085. <https://doi.org/10.1121/1.2336751>

- Sahling, H., Römer, M., Pape, T., Bergès, B., dos Santos Ferreira, C., Boelmann, J., . . . Bohrmann, G. (2014). Gas emissions at the continental margin west of Svalbard: Mapping, sampling, and quantification. *Biogeosciences*, *11*, 6029–6046. <https://doi.org/10.5194/bg-11-6029-2014>
- Sarkar, S., Berndt, C., Minshull, T. A., Westbrook, G. K., Klaeschen, D., Masson, D. G., . . . Thatcher, K. E. (2012). Seismic evidence for shallow gas-escape features associated with a retreating gas hydrate zone offshore west Svalbard. *Journal of Geophysical Research*, *117*, B09102. <https://doi.org/10.1029/2011JB009126>
- Schauer, U., Fahrback, E., Osterhus, S., & Rohardt, G. (2004). Arctic warming through the Fram Strait: Oceanic heat transport from 3 years of measurements. *Journal of Geophysical Research*, *109*, C06026. <https://doi.org/10.1029/2003JC001823>
- Shakhova, N., Semiletov, I., Salyuk, A., Yusupov, V., Kosmach, D., & Gustafsson, Ö. (2010). Extensive methane venting to the atmosphere from sediments of the East Siberian Arctic Shelf. *Science*, *327*, 1246–1250. <https://doi.org/10.1126/science.1182221>
- Simon, M., Stafford, K. M., Beedholm, K., Lee, C. M., & Madsen, P. T. (2010). Singing behavior of fin whales in the Davis Strait with implications for mating, migration and foraging. *Journal of the Acoustical Society of America*, *128*, 3200–3210. <https://doi.org/10.1121/1.3495946>
- Širović, A., Hildebrand, J. A., Wiggins, S. M., McDonald, M. A., Moore, S. E., & Thiele, D. (2004). Seasonality of blue and fin whale calls and the influence of sea ice in the Western Antarctic Peninsula. *Deep Sea Research Part II*, *51*, 2327–2344. <https://doi.org/10.1016/j.dsr2.2004.08.005>
- Sohn, R. A., Hildebrand, J. A., Webb, S. C., & Fox, C. G. (1995). Hydrothermal microseismicity at the megaplume site on the southern Juan de Fuca Ridge. *Bulletin of the Seismological Society of America*, *85*, 775–786.
- Spielhagen, R. F., Werner, K., Sørensen, S. A., Zamelczyk, K., Kandiano, E., Budeus, G., . . . Hald, M. (2011). Enhanced modern heat transfer to the Arctic by warm Atlantic water. *Science*, *331*, 450–453. <https://doi.org/10.1126/science.1197397>
- Steinle, L., Graves, C. A., Treude, T., Ferré, B., Biastoch, A., Bussmann, I., . . . Niemann, H. (2015). Water column methanotrophy controlled by a rapid oceanographic switch. *Nature Geoscience*, *8*, 378–382. <https://doi.org/10.1038/ngeo2420>
- Stewart, I. S., Sauber, J., & Rose, J. (2000). Glacio-seismotectonics: Ice sheets, crustal deformation and seismicity. *Quaternary Science Reviews*, *19*, 1367–1389. [https://doi.org/10.1016/S0277-3791\(00\)00094-9](https://doi.org/10.1016/S0277-3791(00)00094-9)
- Stork, A. L., Verdon, J. P., & Kendall, J.-M. (2015). The microseismic response at the In Salah Carbon Capture and Storage (CCS) site. *International Journal of Greenhouse Gas Control*, *32*, 159–171. <https://doi.org/10.1016/j.ijggc.2014.11.014>
- Sultan, N., Riboulot, V., Ker, S., Marsset, B., Géli, L., Tary, J. B., . . . Grimaud, S. (2011). Dynamics of fault-fluid-hydrate system around a shale-colored anticline in deepwater Nigeria. *Journal of Geophysical Research*, *116*, B12110. <https://doi.org/10.1029/2011JB008218>
- Svendsen, J. I., Mangerud, J., Elverhøi, A., Solheim, A., & Schüttenhelm, R. T. E. (1992). The late Weichselian glacial maximum on western Spitsbergen inferred from offshore sediment cores. *Marine Geology*, *104*, 1–17. [https://doi.org/10.1016/0025-3227\(92\)90081-R](https://doi.org/10.1016/0025-3227(92)90081-R)
- Tanase, D., Sasaki, T., Yoshii, T., Motohashi, S., Sawada, Y., Aramaki, S., . . . Inowaki, R. (2013). Tomakomai CCS demonstration project in Japan. *Energy Procedia*, *37*, 6571–6578. <https://doi.org/10.1016/j.egypro.2013.06.589>
- Tary, J. B., Géli, L., Guennou, C., Henry, P., Sultan, N., Çağatay, N., & Vidal, V. (2012). Microevents produced by gas migration and expulsion at the seabed: A study based on sea bottom recordings from the Sea of Marmara. *Geophysical Journal International*, *190*, 993–1007. <https://doi.org/10.1111/j.1365-246X.2012.05533.x>
- Thatcher, K. E., Westbrook, G. K., Sarkar, S., & Minshull, T. A. (2013). Methane release from warming-induced hydrate dissociation in the West Svalbard continental margin: Timing, rates, and geological controls. *Journal of Geophysical Research: Solid Earth*, *118*, 22–38. <https://doi.org/10.1029/2012JB009605>
- Thompson, P. O., Findley, L. T., & Vidal, O. (1992). 20-Hz pulses and other vocalizations of fin whales, *Balaenoptera physalus*, in the Gulf of California, Mexico. *Journal of the Acoustical Society of America*, *92*, 3051–3057. <https://doi.org/10.1121/1.404201>
- Torres, M. E., McManus, J., Hammond, D. E., de Angelis, M. A., Heeschen, K. U., Colbert, S. L., . . . Suess, E. (2002). Fluid and chemical fluxes in and out of sediments hosting methane hydrate deposits on Hydrate Ridge, OR, I: Hydrological provinces. *Earth Planetary Science Letters*, *201*, 525–540. [https://doi.org/10.1016/S0012-821X\(02\)00733-1](https://doi.org/10.1016/S0012-821X(02)00733-1)
- Trnkoczy, A. (2012). Understanding and parameter setting of STA/LTA trigger algorithm. In P. Bormann (Ed.), *New manual of seismological observatory practice 2 (NMSOP-2)* (pp. 1–20). Potsdam, Germany: Deutsches GeoForschungsZentrum GFZ. https://doi.org/10.2312/GFZ.NMSOP-2_IS_8.1
- Vanneste, M., Guidard, S., & Mienert, J. (2005). Bottom-simulating reflections and geothermal gradients across the western Svalbard margin. *Terra Nova*, *17*, 510–516. <https://doi.org/10.1111/j.1365-3121.2005.00643.x>
- Veloso, M., Greinert, J., Mienert, J., & De Batist, M. (2015). A new methodology for quantifying bubble flow rates in deep water using split-beam echosounders: Examples from the Arctic offshore NW-Svalbard. *Limnology and Oceanography Methods*, *13*, 267–287. <https://doi.org/10.1002/lom3.10024>
- Watkins, W. A., Tyack, P., Moore, K. E., & Bird, J. E. (1987). The 20-Hz signal of finback whales (*Balaenoptera physalus*). *Journal of the Acoustical Society of America*, *82*, 1901–1912. <https://doi.org/10.1121/1.395685>
- Weirathmueller, M. J., Wilcock, W. S. D., & Soule, D. C. (2013). Source levels of fin whale 20 Hz pulses measured in the Northeast Pacific Ocean. *Journal of the Acoustical Society of America*, *133*, 741–749. <https://doi.org/10.1121/1.4773277>
- Westbrook, G. K., Thatcher, K. E., Rohling, E. J., Piotrowski, A. M., Pälke, H., Osborne, A. H., . . . Aquilina, A. (2009). Escape of methane gas from the seabed along the West Spitsbergen continental margin. *Geophysical Research Letters*, *36*, L15608. <https://doi.org/10.1029/2009GL039191>
- Wilcock, W. S. D. (2012). Tracking fin whales in the northeast Pacific Ocean with a seafloor seismic network. *Journal of the Acoustical Society of America*, *132*, 2408–2419. <https://doi.org/10.1121/1.4747017>